Bulletin of the Seismological Society of America, Vol. 101, No. 5, pp. 2369–2387, October 2011, doi: 10.1785/0120100298

Stress Drop during Earthquakes: Effect of Fault Roughness Scaling

by Thibault Candela, François Renard,* Michel Bouchon,
Jean Schmittbuhl, and Emily E. Brodsky

Abstract We propose that a controlling parameter of static stress drop during an earthquake is related to the scaling properties of the fault-surface topography. Using high resolution laser distance meters, we have accurately measured the roughness scaling properties of two fault surfaces in different geological settings (the French Alps and Nevada). The data show that fault-surface topography is scale dependent and may be accurately described by a self-affine geometry with a slight anisotropy characterized by two extreme roughness exponents (H_R), $H_{||} = 0.6$ in the direction of slip and $H_{\perp} = 0.8$ perpendicular to slip.

Disregarding plastic processes like rock fragmentation and focusing on elastic deformation of the topography, which is the dominant mode at large scales, the stress drop is proportional to the deformation, which is a spatial derivative of the slip. The evolution of stress-drop fluctuations on the fault plane can be derived directly from the self-affine property of the fault surface, with the length scale (λ) as $\mathrm{std}_{\Delta\sigma}(\lambda) \propto \lambda^{H_R-1}$.

Assuming no characteristic length scale in fault roughness and a rupture cascade model, we show that as the rupture grows, the average stress drop, and its variability should decrease with increasing source dimension. That is for the average stress drop $\Delta\sigma(r) \propto r^{H_R-1}$, where r is the radius of a circular rupture. This result is a direct consequence of the elastic squeeze of fault asperities that induces the largest spatial fluctuations of the shear strength before and after the earthquake at local (small) scales with peculiar spatial correlations.

Introduction

One of the most commonly used source parameters in the interpretation of earthquakes is the static stress drop ($\Delta\sigma$), which measures the stress decrease after an earthquake, averaged over the rupture surface area (Aki, 1967; Scholz, 2002). A controversial question about stress drop is its dependence or independence with respect to the seismic moment (M_0). Self-similar models of earthquakes (i.e., scale invariance property of earthquake source mechanics) imply that small and large earthquakes are similar in terms of their rupture physics; and as a consequence, stress drop should be independent of earthquake size. This has been proposed in many studies in which earthquake stress drop is generally described as independent of source dimension and seismic moment (Aki, 1967; Kanamori and Anderson, 1975; Hanks, 1977; Abercrombie, 1995; Ide *et al.*, 2003; Kanamori and Brodsky, 2004; Prieto *et al.*, 2004; Abercrombie and Rice, 2005; Imanishi and Ellsworth, 2006; Shearer *et al.*, 2006).

However, the wide dispersion of commonly accepted values of static stress drop calls into question the assumption that earthquake source properties are in fact scale invariant. The scatter of static stress-drop values versus seismic moment originates partly from unmodeled sources of error such as directivity effect (Bernard *et al.*, 1996; Imanishi and Ellsworth, 2006) or near-surface attenuation (Hanks, 1982; Anderson and Hough, 1984; Anderson, 1986). Indeed corrections for path and site response effects need to be applied before determining the source radius and the stress drop (Frankel and Wenneberg, 1989; Boatwright *et al.*, 1991). However, other studies suggest that heterogeneous properties in faulting influence the value of static stress drop and propose that source factors do account for the observed variability (Choy and Kirby, 2004; Venkataraman and Kanamori, 2004). Singh and Suárez (1988) report a correlation between low stress drops and the smaller number of aftershocks in the Cocos subduction zone in Central America compared to a global average. They proposed that variations in the smoothness of the seafloor topography may be a possible cause. R. M. Harrington and E. E. Brodsky (2011, personal comm.) have observed that small earthquakes on immature faults obey the energy scaling expected for constant stress drop (self-similar model), while those of mature faults do not. Based on the estimations of source parameters from a spectra of 42,367 earthquakes between 1984 and 2005, Allmann and

*Also at Physics of Geological Processes, University of Oslo, Oslo, Norway.

Shearer (2007) indicate that the patterns of high and low stress-drop regions on the San Andreas fault (California) remain largely unchanged by the occurrence of the 2004 M 6.0 Parkfield earthquake. These authors suggest that stress drops are mainly controlled by rock properties and that strong heterogeneities of the stress field persist along the fault over the seismic cycle. This picture is also supported by the observation that the aftershocks of the Parkfield earthquake are distributed along the same trace and display the same seismicity holes as the background before the mainshock (Allmann and Shearer, 2007).

In the present study, we propose that a controlling parameter of the static stress drop is related to the scale properties of the topography of the fault surface (i.e., fault roughness). Combining new fault roughness measurements with a recent study (Schmittbuhl *et al.*, 2006) that links the fault-surface morphology with the shear strength along the fault plane and using a numerical model of fault propagation (Schmittbuhl and Vilotte, 1999; Candela *et al.*, 2011, unpublished manuscript) we deduce that fault geometry controls slip fluctuations on the fault plane. Given the close relationship between slip and stress drop, we infer the evolution of the spatial fluctuations of the stress drop on the fault plane as a function of the length scale. Therefore, considering that an earthquake is composed of a hierarchical set of smaller earthquakes, we propose a theoretical scaling model for the average static stress drop and its variability that is directly associated with the scale property of the fault surface. This scaling model is developed in the framework of a rupture cascade model.

In the first part of this paper, we present new analysis of fault roughness illustrating a unique identical self-affine property regardless of the geological setting (various accumulated displacement, host rock, and slip movement). In the second part, we present the scaling of the spatial variability of the stress drop along the rupture surface. In the third part, we infer the evolution of the average stress drop and its variability as a function of the earthquake size by applying a rupture cascade model. Our scaling relationships are applied on the Nojima fault plane (1995 M 7 Kobe earthquake) for which the stress pattern along the fault plane could be imaged before and after the earthquake (Bouchon *et al.*, 1998). We extrapolate the spatial fluctuations of the stress drop toward smaller scale after the Kobe earthquake, and infer the average stress drop and its variability for small earthquakes along the fault.

Roughness of Natural Fault Surfaces

Definition of Scaling Properties and the Hurst Exponent

We first recall some definitions related to the scaling properties of a rough signal. A self-affine 2D signal (Fig. 1) remains unchanged under the scaling transformation $\delta x \rightarrow \lambda \delta x$ and $\delta z \rightarrow \lambda^{H_R} \delta z$ (Meakin, 1998). Here δx is the coordinate along the 2D profile, and δz is the roughness amplitude. For a self-affine profile, the scaling exponent H_R, also called the Hurst exponent (or roughness exponent), lies in the range $0 \leq H_R \leq 1$. In the particular case where $H_R = 1$, the profile obeys a self-similar description: a small portion of it, when magnified isotropically, has a statistically identical appearance to a larger part of the profile. Conversely, if a profile is best fitted with a self-affine model ($0 \leq H_R < 1$), different magnification factors will be needed for the directions parallel and perpendicular to the profile for a small portion of it to appear statistically similar to the entire profile (Fig. 1). As a consequence, the slope along a self-affine profile follows a scaling such that $s = \delta z / \delta x \, \alpha \, \delta x^{H_R - 1}$ and tends to flatten for long wavelengths (Fig. 1). Accordingly, as opposed to self-similar surfaces, this shows that the profile roughness is flatter at large scales but still includes a large variety of patterns of small amplitude asperities.

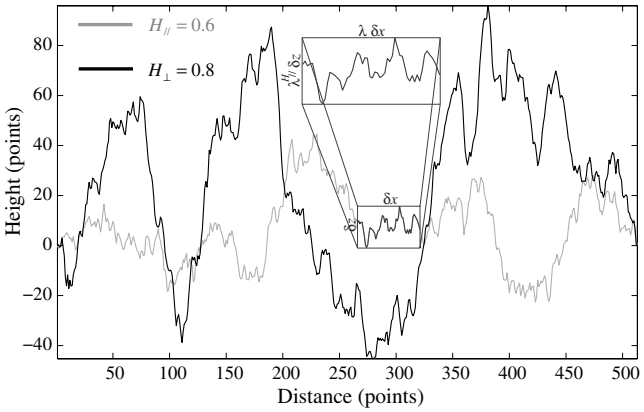

Figure 1. Representative 2D synthetic self-affine profiles computed with Hurst exponents $H_{||} = 0.6$ and $H_{\perp} = 0.8$. We use a Fourier-based method to simulate both self-affine profiles (Candela *et al.*, 2009). The profile parallel to slip (with the smallest Hurst exponent) appears jagged at small scales and smooth at large scales, compared to the profile normal to slip. Inset: magnified portion of the profile along slip, which has a statistically similar appearance to the entire profile when using the rescaling transformation $\delta x \rightarrow \lambda \delta x$, $\delta z \rightarrow \lambda^{H_{||}} \delta z$.

Fault Roughness Scaling

Despite recent progress in seismology, the imaging of fault planes over a large range of scales at depth is not yet available. A quasi-unique access to the high-resolution description of the fault plane comes from exhumed fault scarp observations. From pioneer measurements of fault-surface topography using a mechanical profilometer, it has been shown that fault roughness is scale invariant with a self-similar character (Power *et al.*, 1987, 1988; Power and Tullis, 1991; Power and Durham, 1997). Two parameters are required to describe a self-similar or self-affine model in the spectral domain: (1) the slope of the power spectrum and (2) its intercept on a log–log plot of power spectral density versus frequency. The slope of the spectrum (directly

proportional to H_R) describes how the roughness changes with scale, while the intercept determines the amplitude of surface elevation at a given scale (Power and Tullis, 1991).

As a result of technical limitations, as pointed out by Power *et al.* (1987), these pioneer analyses performed mainly with 2D profilometers did not give access to slight variations of the slope of the spectrum because of the large variability and errors introduced by the sporadic sampling of the whole fault scarp. Consequently, these studies have focused their efforts on the intercept and concluded that an obvious and expected consequence of slip-related striations on fault planes is that profiles parallel to slip have lower spectral densities than those normal to slip, whereas the slope is roughly identical in both directions and follows an average self-similar regime (Power *et al.*, 1987, 1988; Power and Tullis, 1991; Power and Durham, 1997).

With the recent development of high-resolution distance meters, it is now possible to use accurate statistical approaches to quantify fault roughness. Indeed, Light Detection And Ranging (LiDAR) portable 3D laser scanners allow mapping the whole fault-surface outcrops over scales from millimeter to several tens of meters (Renard *et al.*, 2006; Sagy *et al.*, 2007; Candela *et al.*, 2009; Brodsky *et al.*, 2011). The accuracy of the measurements enables a reliable quantification of the data. Renard *et al.* (2006) and Candela *et al.* (2009) demonstrated precisely the anisotropic self-affine properties of fault topography using ground-based LiDAR and laboratory profilometers. They showed that both slope and intercept are lower in the direction of slip than perpendicular to it.

Self-Affine Geometry of the Vuache and Dixie Valley Fault Scarps

In addition to previously published data acquired on the Vuache fault (Renard *et al.*, 2006; Candela *et al.*, 2009), we include new measurements performed on the Dixie Valley fault surface (Table 1), where a neighboring fault scarp has been studied by Power *et al.* (1987) and Power and Tullis (1992). The aim of this section is to compare two faults in different geological settings and to quantify their roughness properties.

The Vuache fault is an active strike-slip fault system in the western part of the French Alps (Thouvenot, 1998) that offsets meter-scale beds of limestones. We consider here a satellite branch of this fault system where the cumulated slip is small, in the range of 10 to 30 m. The fault plane was exhumed ten years ago by the activity of a quarry. As a consequence, the LiDAR measurements could be performed on fresh surfaces, where weathering was minimal and the surfaces were vegetation free.

The Dixie Valley (Nevada) fault surface has a mainly normal slip component and cuts through rhyolites. The high resistance of rhyolite (composed mainly of quartz) to weathering and the dry climate of the Nevada desert allow excellent preservation of the slip surfaces (Fig. 2a). The Dixie Valley fault consists of many discrete slip surfaces at all scales separating lenses of variably deformed fault rock. Although normal cumulated slip for the fault zone as a whole in the study area is 3–6 km (Okaya and Thompson, 1985; Fonseca, 1988; Power and Tullis, 1989), individual surfaces within the fault zone have experienced considerably less slip.

Three different models of LiDAR apparatus were used to acquire digital elevation models (DEMs) of the fault roughness with a height resolution down to one centimeter. A Leica HDS3000 was used for the Dixie Valley fault, and both a RIEGL LMS Z420i and a Trimble GS100 were used for the Vuache fault (Table 1). For each fault, several patches of the surface were scanned at a resolution from 5 to 30 mm, which is coarser than the precision of the scanners, and constituted individual DEMs for which size lies between 1 and 170 m^2. In Figure 2b, we show one example of a DEM extracted from the Dixie Valley fault surface. DEMs of the Vuache fault surface are presented in Candela *et al.* (2009).

The Hurst exponent H_R can be estimated from the Fourier power spectrum, which has a power law form for a 2D self-affine profile (Barabasi and Stanley, 1995; Meakin, 1998). First, linear detrending is performed independently on all the profiles selected in a given direction from a DEM

Table 1
Laser Scanner Characteristics and Fault Roughness Results

DEM*	Scanner	Resolution	Noise on the Data	$H_{\|\|}$ † (±0.05)	$H_{\perp}$ ‡ (±0.05)
Vuache Fault, 45°57′14.5″ N, 6°2′56″ E					
Surf-1	GS 100 (Trimble)	20 mm	4.5 mm	0.59	0.79
Surf-7	GS 100 (Trimble)	20 mm	4.5 mm	0.68	0.84
Surf-6	LMS Z420i (Riegl)	30 mm	10.2 mm	0.5	0.81
Dixie Valley Fault, 39°56′48″ N, 117°56′43″ E					
Dixie Valley-1	HDS3000 (Leica)	5 mm	2 mm	0.66	0.78
Dixie Valley-2	HDS3000 (Leica)	5 mm	2 mm	0.63	0.79
Dixie Valley-3	HDS3000 (Leica)	5 mm	2 mm	0.60	0.83
Dixie Valley-4	HDS3000 (Leica)	5 mm	2 mm	0.46	0.84

*DEM, Digital Elevation Model
†Average $H_{||}$ for the Vuache fault: 0.59 ± 0.09. Average $H_{||}$ for the Dixie Valley fault: 0.59 ± 0.08.
‡Average $H_{\perp}$ for the Vuache fault: 0.81 ± 0.02. Average $H_{\perp}$ for the Dixie Valley fault: 0.81 ± 0.04.

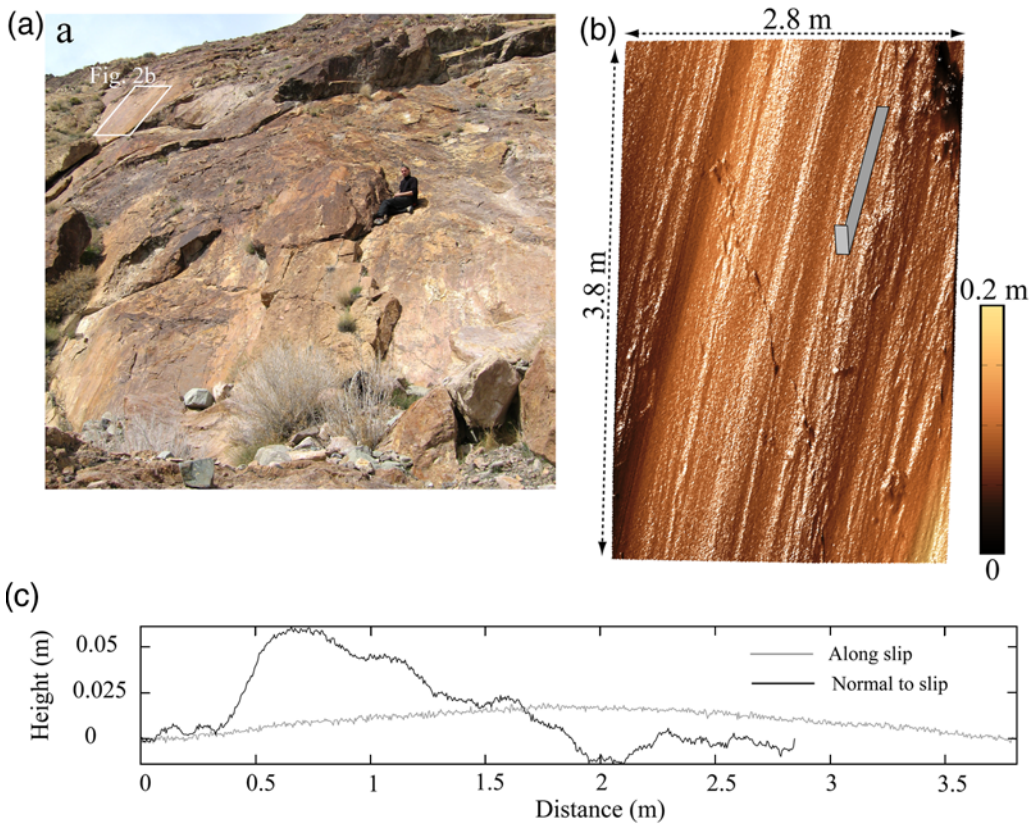

Figure 2. Dixie Valley fault-surface topography. (a) Whole outcrop, constituted by many discrete slip surfaces. The inset corresponds to the surface shown in (b). (b) Enlargement on the fault, which corresponds to the digital elevation model (DEM) labeled Dixie Valley-2 in Table 1. (c) Representative 2D self-affine profiles of the slip surface extracted from (b) the DEM in the direction of slip and perpendicular to it. The color version of this figure is available only in the electronic edition.

(Fig. 2c). Next, for each parallel detrended profile in the direction of slip and those perpendicular to the slip direction (Fig. 1), the Fourier power spectrum $P(k)$ (i.e., the square of the modulus of the Fourier transform) is calculated as a function of wavenumber k. Then the spectrum of each DEM is calculated by stacking and averaging all 2D Fourier transforms to reduce the noise associated with individual profiles. Each DEM gives one spectrum. Three similar spectra were computed from the three DEMs for the Vuache fault surface, and four were computed from the four DEMs for the Dixie Valley fault surface. These spectra were then coarse-grained and averaged to recover the general trend of each surface (Fig. 3 and Table 1). When representing the Fourier power spectrum as a function of wavenumber in a log–log plot, a self-affine function reveals a linear slope, which is itself a function of H_R through $P(k) \propto k^{-1-2H_R}$. In Figure 3, Fourier power spectra are displayed for the slip direction and normal to slip, showing the two extreme self-affine regimes characterizing fault topography, as suggested by Candela *et al.* (2009). Note that these scaling relationships flatten at length-scales below ~10 cm for the Vuache fault and ~2 cm for the Dixie Valley fault. This is due to the noise inherent in the measurement using the LiDAR apparatus. This noise level varies between the three instruments we used and was in the range of 2 to 10 mm (see Table 1).

Our results clearly highlight an identical directional morphological self-affine anisotropy for both fault-surface geometries (Fig. 3). All the power-law fits performed for each sub-surface (or DEM) to extract each roughness exponent are presented in Table 1. The surface geometry of the Vuache and Dixie Valley faults can be accurately described by two scaling roughness Hurst exponents H_R in both structural directions. These are $H_{||} = 0.59 \pm 0.09$ and $H_{\perp} = 0.81 \pm 0.02$ for the Vuache fault and $H_{||} = 0.59 \pm 0.08$ and $H_{\perp} = 0.81 \pm 0.04$ for the Dixie Valley fault. The structural slip direction, highlighted by linear striations at small scales, and the perpendicular direction correspond roughly to the two directions where the estimated self-affine exponents are the smallest and the largest, respectively. The compiled results of this analysis and previous works (Schmittbuhl *et al.*, 1993; Lee and Bruhn, 1996; Renard *et al.*, 2006; Candela *et al.*, 2009) show that despite different geological settings (various accumulated displacement, host rock, and slip movement), an anisotropic self-affine model may describe accurately fault asperity geometry. The roughness exponents H_R are in the range of 0.6 to 0.8 (i.e., self-affine

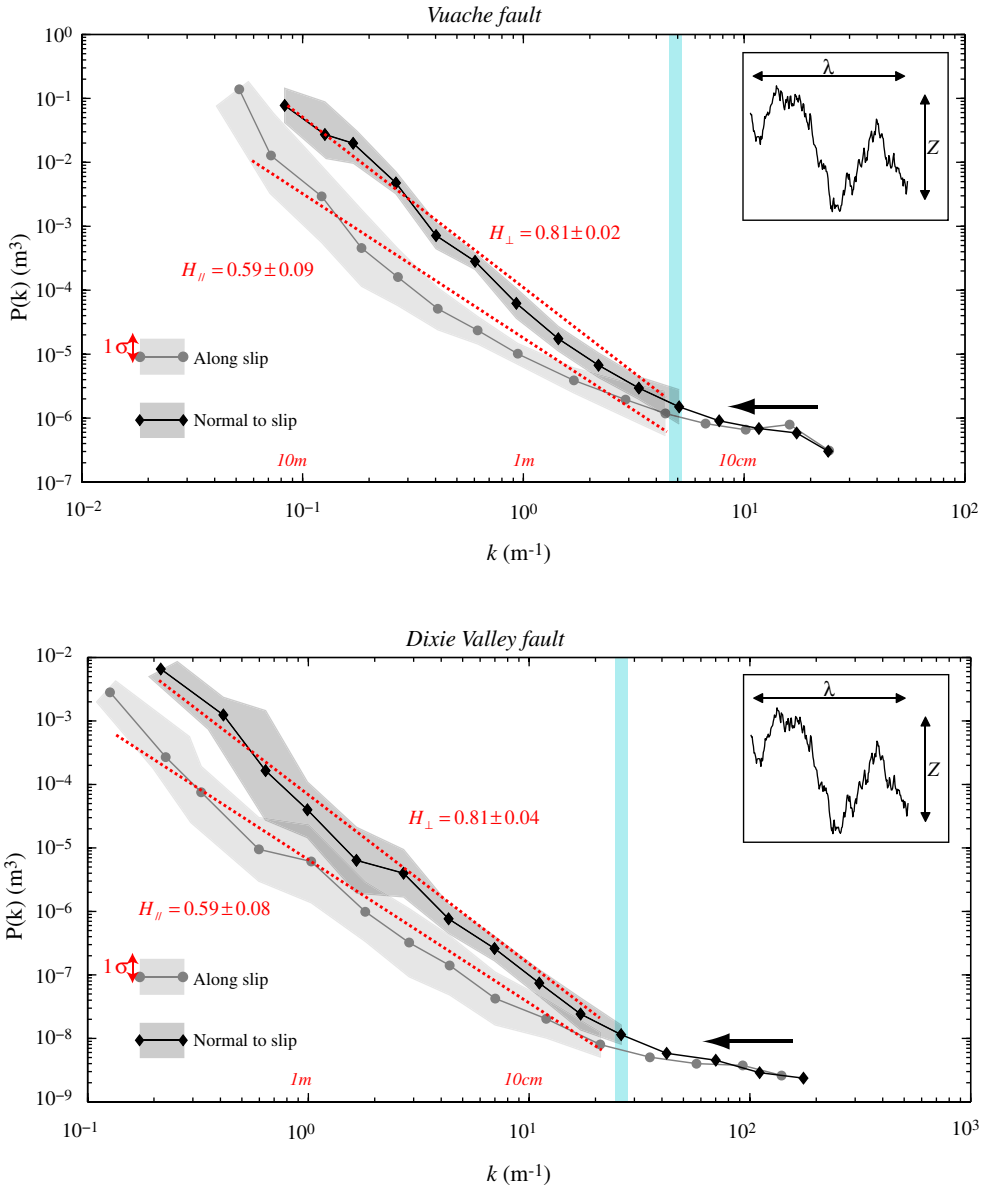

Figure 3. Fourier power spectrum calculated for the Vuache and Dixie Valley fault surfaces along and perpendicular to slip directions and their respective standard deviations. The data collected contain three and four surfaces of the Vuache and Dixie Valley fault surfaces, respectively, that have been scanned using ground-based LiDAR. Power-law fits (dotted lines) are shown on plots for ease of comparison. The vertical bars indicate the upper limits of the wavenumbers used for fitting. The insets display an example of the height elevation Z ($\sim y$-axis) vs. wavelength $\lambda = 1/k$ ($\sim x$-axis) of a rough profile. The level of noise is indicated by the arrows. The color version of this figure is available only in the electronic edition.

case) and always smaller than 1 (i.e., self-similar case) in both structural directions. The two faults studied were exhumed from shallow depths (<5 km). Their topography has recorded both the propagation and termination of major earthquakes ruptures that initiate at greater depths. It is worth noting that in a recent work (Bistacchi *et al.*, 2011) the same self-affine regime was measured on the Gole Larghe fault zone (Italian Alps). This fault has recorded slip processes at the depth of seismogenic nucleation. One may conclude that the self-affine geometrical model may represent a global feature of natural fault surfaces.

Spatial Variability of the Stress Drop on the Fault Plane

Relationship between Slip and Fault Roughness

In their asperity squeeze model, Schmittbuhl *et al.* (2006) have proposed that fluctuations of the frictional shear-strength field can be understood as the expression of two self-affine fault planes pressed together elastically and sheared with frictional sliding (i.e., at the Coulomb threshold). In the approximations by Schmittbuhl *et al.* (2006) of full contact of the fault planes and elastic deformation of the

topography, frictional shear strength distribution constitutes an intrinsic property of the fault plane and is only slightly affected by dynamic stress fluctuations produced during the earthquake. Accordingly, the Hurst exponent H_{τ_i}, characterizing the self-affinity of the shear-strength field before the earthquake, approaches

$$H_{\tau_i} = H_R - 1. \quad (1)$$

In addition, Schmittbuhl and Vilotte (1999), using a numerical model of quasi-static tensile crack propagation, have demonstrated that the interactions between toughness heterogeneities and elastic stress transfers lead to nontrivial spatiotemporal correlations of slip. Indeed, neglecting any dynamic effects due to stress overshoots, inertia, or wave effects, they show that, for long-range correlations of toughness heterogeneities characterized by a self-affine exponent H_t, the roughness exponent of the slip distribution follows the scaling $H_s = H_t + 1$ for a wide range of values of H_t between -1 and $+1$. The results obtained with this numerical model developed for mode I ruptures can be extended to mode II or III ruptures, which are relevant for the description of shear fault rupture during earthquakes (Schmittbuhl *et al.*, 2003; Candela *et al.*, 2011). The toughness disorder in the case of mode I rupture propagation is then converted into frictional disorder for mode II or III ruptures and

$$H_s = H_{\tau_i} + 1, \quad (2)$$

with H_{τ_i} characterizing the long-range correlations of the frictional shear strength (such as due to asperities) along the fault plane before the rupture. Finally, combining equations (1) and (2), it follows that

$$H_R = H_s, \quad (3)$$

showing that self-affine geometrical properties of fault-surface roughness may control slip correlations. Even if the quasi-static model of fault propagation discussed here neglects any dynamic effect inherent to rapid coseismic slip, we emphasize that the spatial slip correlations observed (equation 3) are consistent with those of seismological slip maps (Mai and Beroza, 2002).

Scaling of the Standard Deviation of the Stress Drop after an Earthquake

Fault Slip Distribution and Stress-Drop Variability. For a 2D scale-invariant model of slip, the Fourier transform of the slip distribution $u(k)$ follows $k^{-1-H_s}\gamma(k)$, with γ being a Gaussian white noise (Marsan, 2006). By definition, for an elastic body the stress drop is proportional to the deformation, which is a spatial derivative of the slip. Therefore, the stress drop scales as $\Delta\sigma(k) \propto ku(k) \propto k^{-H_s}\gamma(k)$ for a wavenumber k (Marsan, 2006), and the scaling of the standard deviation $std_{\Delta\sigma}(\lambda)$ of the stress drop at scale λ is given by

$$std^2_{\Delta\sigma}(\lambda) \propto \int_{1/L}^{1/\lambda} dkk|\Delta\sigma(k)|^2 \Rightarrow \mathrm{std}_{\Delta\sigma}(\lambda) \propto \left[\left(\frac{L}{\lambda}\right)^{2-2H_s} - 1\right]^{1/2} \quad (\text{for } H_s < 1), \quad (4)$$

where L is the size (total length) of the coseismic rupture. In the limit $\lambda \to 0$,

$$std_{\Delta\sigma}(\lambda) \propto \lambda^{H_s-1}. \quad (5)$$

Note that when reaching small wavelengths, the standard deviation of the stress drop should diverge. There, the elastic assumption is not relevant anymore because plastic deformation must take place to dissipate the largest stress concentrations (Dieterich and Smith, 2009).

As suggested in the previous paragraph, spatial slip correlations are directly linked to the distribution of fault asperities. Combining equations (4) and (5) with equation (3) we obtain, for $H_R < 1$,

$$std_{\Delta\sigma}(\lambda) \propto \left[\left(\frac{L}{\lambda}\right)^{2-2H_R} - 1\right]^{1/2}, \quad (6)$$

and in the limit $\lambda \to 0$ we obtain

$$std_{\Delta\sigma}(\lambda) \propto \lambda^{H_R-1}, \quad (7)$$

indicating that the evolution of the stress-drop standard deviation with the length-scale λ may be controlled by fault geometrical properties. In other words, the variability of the stress drop along the fault plane after an earthquake should increase toward small scales because of the self-affine character of the fault surface ($H_R < 1$). Note that in the case of a self-similar fault roughness, stress fluctuations would be of the same intensity at all scales. Figure 4 displays this standard deviation $std_{\Delta\sigma}(\lambda)$ for H_R, ranging from 0.6 to 0.8, as

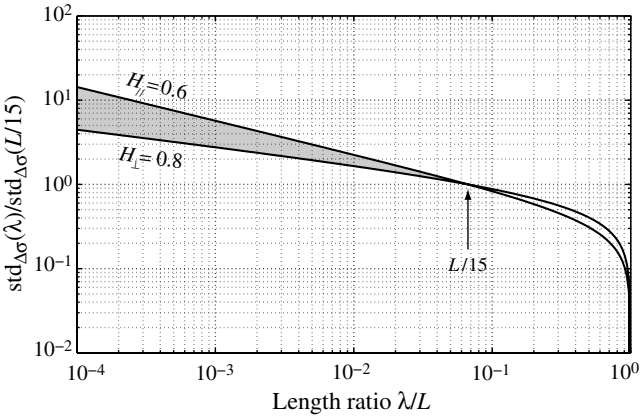

Figure 4. Increase of $\mathrm{std}_{\Delta\sigma}(\lambda)$, the stress-drop variability (standard deviation) at scale λ, with the decrease of λ for the range of Hurst exponents H_R given by fault roughness analyses ($H_{||} = 0.6$, $H_{\perp} = 0.8$). This graph represents the generic case of a rupture of total length L for which the stress-drop variability is known from seismological slip inversions down to scale $L/15$. Such a scale is generally close to ~4 km, corresponding to an ~60 -km-long rupture (i.e., a magnitude ~7 event, analogous to the 1995 Kobe earthquake).

given by equation (6). Considering the two H_R end members obtained in the fault roughness analysis ($H_{||} = 0.6$ and $H_{\perp} = 0.8$), we illustrate the scaling of the standard deviation of the stress drop on a rupture surface of total length $L =$ 60 km, when the stress-drop variability is known down to the scale of 4 km, as is generally obtained by seismological slip inversions. In other words, we extrapolate at small scales the stress-drop variability on a fault surface caused by a magnitude ~7 earthquake (analogous to the Kobe earthquake).

Absolute Shear Stress and Stress-Drop Variability

Analogy between the Stress Drop and the Fracture Aperture Scaling

In the previous section, Relationship between Slip and Fault Roughness, the shear-strength field before the rupture is directly linked to fault topography by the asperity squeeze model (Schmittbuhl *et al.*, 2006). In the same way, this model implies that the state of stress after an earthquake is controlled by fault roughness and is only slightly affected by the dynamic effects during the rupture propagation, at least when considering its scaling properties. In this framework, the only way to alter the final strength distribution is to modify the fault morphology during the slip event. Therefore, the relationship established in equation (1) could be applied for both the initial and final shear strength, and the scaling of their standard deviations at a given length scaleλ evolves as

$$std_{\tau_i,\tau_f}(\lambda) \propto \lambda^{H_R-1}, \tag{8}$$

where τ_f corresponds to the final shear strength. If one assumes that the stress drops quasi-statically from the initial shear strength τ_i (which can be interpreted as the yield stress) to the final shear strength (i.e., the final loading stress), then the static stress drop after an earthquake can be defined as $\Delta\sigma = \tau_i - \tau_f$. To derive the scaling of its variability, we make the analogy with the scaling of the fracture aperture (Méheust and Schmittbuhl, 2003). Indeed in our case, each facing fracture surface mimics the initial and final shear strength. Two situations are possible: (1) both self-affine surfaces display fluctuations uncorrelated with each other at all scales, or (2) they are matched at large scales but uncorrelated at small scales. In the first situation, the difference of the two self-affine surfaces (the fracture aperture or the stress drop) is also self-affine with an identical Hurst exponent, but in the second situation, at large scales where both surfaces are matched, their difference appears smooth and does not preserve the self-affine regime still present at smaller scales.

Application to the 1995 Kobe Earthquake

It has been possible to reconstruct not only the stress drop, but also the absolute stress field for the 1995 Kobe, Japan, earthquake (Nojima fault) (Bouchon *et al.*, 1998). This is a unique case that gives the opportunity to test both previous possibilities and infer the scaling of the stress-drop variability in a different and independent way from that proposed previously in the Fault Slip Distribution and Stress-Drop Variability section. In Figure 5a, the shear-stress maps from before and after the Kobe earthquake show persistent spatial fluctuations (Bouchon *et al.*, 1998): relative maxima are located at similar positions along the fault plane, except at large depths.

Before analyzing precisely the spatial distributions and, more especially, the possible spatial correlations of the absolute stress field and the stress drop of the Kobe earthquake, it is important to clarify some points on the reliability of a model derived from an inversion. Indeed, even if inversions of the same rupture event show discrepancies, Mai and Beroza (2002) found, in their extended analysis of spatial correlations of slip maps for 44 earthquakes, that they follow a self-affine regime characterized by an average value $H_s = 0.71 \pm 0.23$. This result, even if it is accompanied by a large standard deviation, demonstrates that the very heterogeneous patterns on slip maps are better fit by a self-affine model (i.e., $H < 1$) than a self-similar model (i.e., $H = 1$). In addition, Causse *et al.* (2010) have recently shown that kinematic inversion methods represent a relevant tool to retrieve the slip roughness even if the smoothing constraints used to stabilize the inversion lead to a slight underestimation of the slip spectrum corner wavenumber.

In the same way we searched for the roughness analysis of fault surfaces, we have searched for possible spatial correlations of the absolute stress field and the stress drop on each map that can be considered reliable despite the small range of resolution. The Fourier power spectrum of each stress map is obtained by averaging the spectra of the individual profiles of the first 10 km of depth (the region of highest resolution). The power spectra of the initial and final stress profiles along the strike direction (Fig. 5b) show an identical self-affine behavior with a negative Hurst exponent $H_{\tau_i,\tau_f} = -0.2 \pm 0.1$ at scales larger than ~4 km, the scale below which spatial smoothing applied for the inversions has an effect. This self-affine behavior is in qualitative agreement with the range of values predicted by the asperity squeeze model. This confirms that an elastic squeeze of fault asperities could explain the spatial distributions of the shear strength along the fault, both before and after the rupture event. Another important result is that the stress-drop spatial distribution follows the same self-affine regime as that for the initial and final stress. This latter observation suggests that even if the initial and final strength maps show persistent spatial fluctuations, they are also uncorrelated with each other at all scales, explaining that their difference (i.e., the stress drop) is also self-affine with an identical negative self-affine Hurst exponent. Indeed, the vertical shift downward of the final shear-stress spectrum compared to the initial shear-stress spectrum, while keeping the same log–log slope, indicates that the roughness amplitude was decreased at all scales but the relative amplitude of the modes of short and large wavelengths remains identical. In other words, and illustrated by profiles extracted from the stress field maps

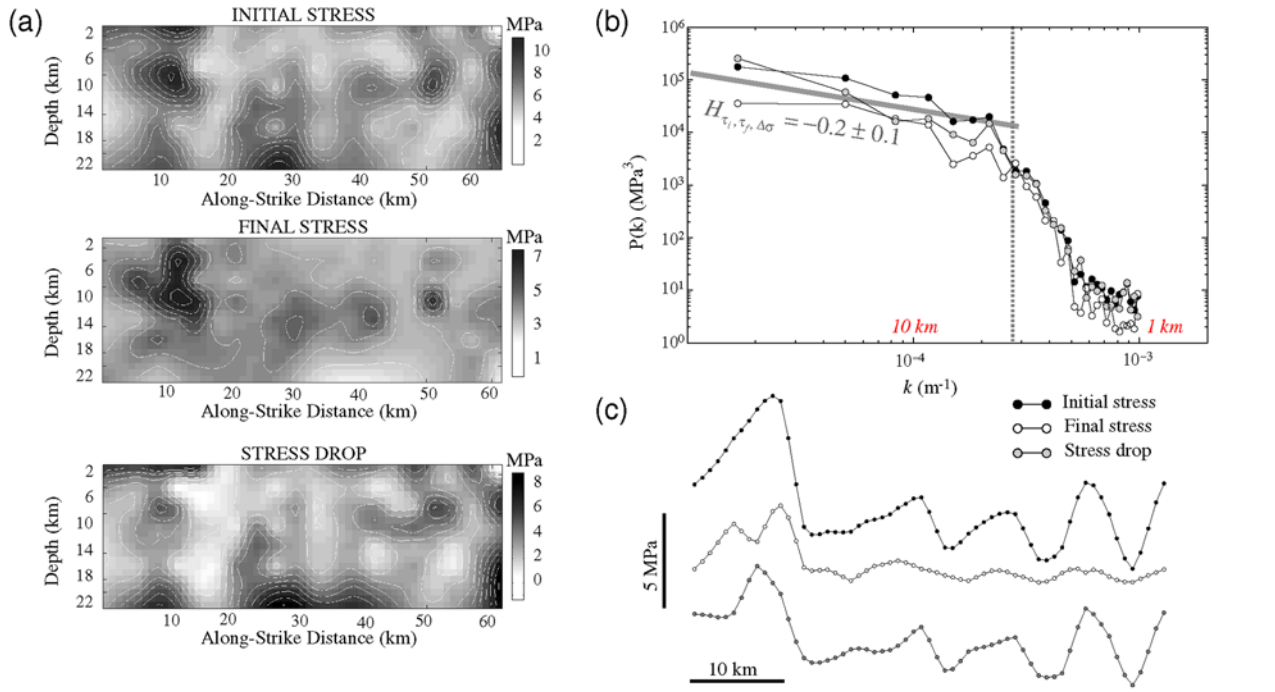

Figure 5. Investigation of the absolute shear strength and the stress-drop variability inferred for the Kobe earthquake. (a) Absolute shear strength and stress drop inferred for the Kobe earthquake (after Bouchon *et al.*, 1998). Above 10 km of depth, these distributions show persistent spatial fluctuations: relative maxima (dark gray areas) are located at similar positions along the fault plane. (b) Fourier power spectrum of the absolute shear strength and stress-drop profiles averaged over the first 10 km of depth in the maps shown in (a). Note that the vertical dashed gray line displays the smallest length scale at which the spatial fluctuations of the stresses are accessible by the seismological inversions (i.e., ~4 km). (c) Profiles extracted at the same position (7 km of depth) for each stress map displayed in (a) showing that fluctuations are larger at small scales than at larger scales, where they appear nearly linear. In addition, persistent spatial fluctuations of relative maxima are clearly identifiable between the initial and the final stress profile even if the overall roughness amplitude of the latter is considerably reduced. The resulting difference of these unmatched initial and final stress profiles (i.e., the stress-drop profile) displays identical fluctuations at all scales conserving the same self-affine regime. The color version of this figure is available only in the electronic edition.

(Fig. 5c), the position of relative maxima (largest asperities) have been preserved, keeping the spatial fluctuations persistent even if at all scales the roughness amplitude has decreased. Finally, given that in the framework of the asperity squeeze model, the stress field before and after the earthquake are the fingerprints of the fault-surface roughness, we suspect that this difference in both stress fields is directly linked to a slight change in fault morphology caused by the rupture event. As suggested by Schmittbuhl *et al.* (2006), it is conceivable that a slight decrease of the roughness amplitude at all scales (while keeping a similar Hurst exponent) caused by the earthquake could contribute to the decreasing of the pre-factor observed for the Kobe final strength. This hypothesis is illustrated in Figure 6 using three synthetic self-affine profiles defined by an identical negative Hurst exponent of −0.2 and three different pre-factors as visualized for the distributions of the shear strength and the stress drop along the Nojima fault plane before and after the Kobe earthquake. In summary, our analysis of the spatial variability of the strength before and after the Kobe earthquake demonstrates that they are uncorrelated mutually at all scales, even if large scale fluctuations are persistent, and confirms that their difference (i.e., the stress drop) scales also with λ, as provided by the scaling relationship in equation (7).

Evolution of the Stress Drop with Rupture Size

Implication of a Rupture Cascade Model on the Variability of the Stress Drop

In the previous section, we demonstrated that as a consequence of $H_R < 1$, the variability of the stress drop after an earthquake increases toward the small scales and large stress drops could be attained at small scales along the fault plane hosting the rupture. Here we propose to deduce the dependence of the average stress drop on rupture size.

In a slip pulse model of an earthquake on a fault with a spatially varying strength, once slip initiates at a point, the fault continues to slide until it encounters a strong barrier (e.g., Brodsky and Mori, 2007). In a different point of view, but not incompatible with the slip pulse model, an earthquake can be conceptualized as a hierarchical cascade of ruptures: an earthquake would be composed of subevents with different sizes, these subevents are themselves composed of subevents, and so on (Frankel, 1991). Note that the propagation of each small earthquake or subevent can follow the slip pulse model.

Based on our analysis of fault-surface morphology, we use a self-affine model of fault roughness on which cascade rupture propagation occurs. For such a model, Andrews

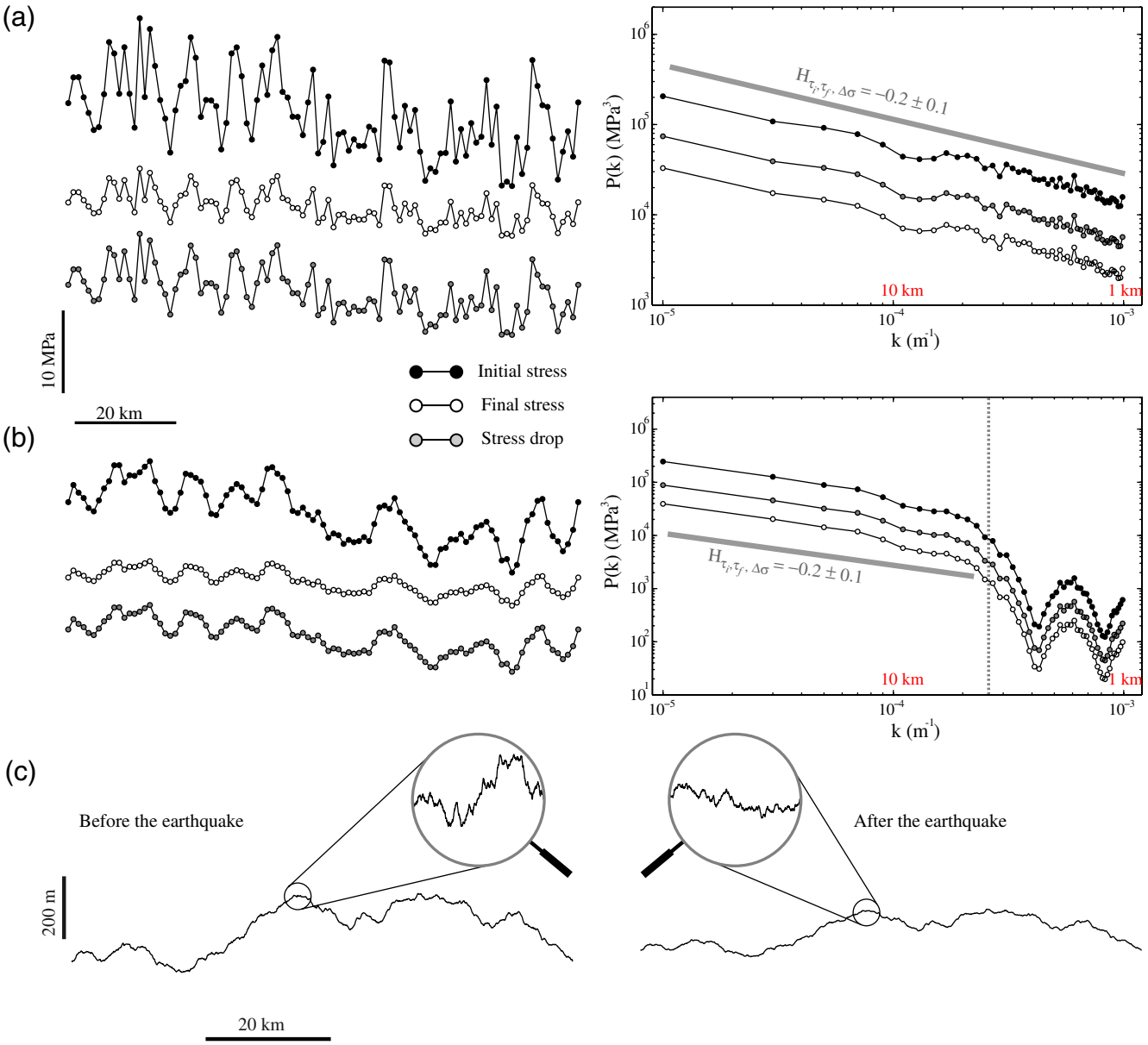

Figure 6. Conceptual model of the difference in the variability of the shear strength before and after the Kobe earthquake. (a) Ideal synthetic self-affine profiles with a prescribed Hurst exponent of −0.2, analogous to the stress field of the Kobe earthquake (shown in Fig. 5) without smoothing inherent to the inversion procedure. The difference between the synthetic initial and final stresses shows a decrease of the roughness amplitude at all scales, preserving the relative importance between large and small scale fluctuations. Persistent spatial fluctuations at large scale are preserved. The stress-drop synthetic profile is also self-affine with an identical negative scaling exponent. At the right, the Fourier power spectra of each profile shows a similar pattern as observed for the Kobe earthquake stress maps (displayed in Fig. 5). (b) Same graph as in (a) except that the ideal synthetic self-affine profiles have been smoothed as observed on seismological slip inversions. Large scale fluctuations are not affected by the smoothing procedure. (c) Difference in the pre-factors of the respective Fourier spectra is directly related to slight variations in fault morphology caused by the rupture event. Two examples of synthetic rough profiles with a prescribed Hurst exponent of 0.8 (analogous to that sampled on natural fault surfaces). The color version of this figure is available only in the electronic edition.

(1980) and Frankel (1991) have suggested that the stress drop could be independent of event size. However, in both works the initial shear strength was implicitly independent of scale ($H_{\tau_i} = 0$). Consequently, in their analysis the average stress drop over a given surface area was independent of the size of the area because the standard deviation of the spatial variations of the initial shear strength was considered constant on the fault plane. In other words, as the rupture propagates, rupture of an asperity (or subevent) removes the spatial fluctuations in shear strength over the dimension of the asperity. Thus the stress drop remains proportional to the standard deviation of the initial shear strength. As in their model, the shear strength was scale independent, therefore each subevent of different size released an equal stress.

In the present study, we have constraints on the stress state before and after the mainshock given directly by the asperity squeeze model and applied for the absolute stress distributions visualized on the Kobe earthquake. The power spectrum modules of the shear-stress distribution of the Kobe earthquake are related to their spatial variability (standard deviation) in order to visualize the two boundary conditions of our problem. Considering that $std_{\tau_i,\tau_f}(\lambda) = \theta\lambda^{H_{\tau_i,\tau_f}}$ and $P_{\tau_i,\tau_f}(k) = \beta k^{-1-2H_{\tau_i,\tau_f}}$, we directly deduce that $\theta = \beta^{1/2}$ with $\lambda = 1/k$. In Figure 7, after extracting the pre-factors of the power law fits performed on the Fourier spectrum of the initial and final shear strength of the Kobe earthquake, we deduce the scaling of the variability of the initial and final shear strengths as a function of the length scale. Considering that each length scale corresponds to subevents of hierarchical size, it is possible to visualize the evolution of the stress drop as a function of the size of the subevents. In the framework of a rupture cascade model, the unique way to obtain the spatial distribution of the initial and final shear strength on the Nojima fault plane is to release the condition of stress proportionality to the initial shear strength at each scale. Indeed, to obtain the final shear strength from the initial one, the stress release is proportional to the initial stress state in order to maintain an identical self-affine regime between the two distributions. Following the same reasoning of Frankel (1991), the stress drop is proportional to the standard deviation of the initial shear strength. As a consequence, the final stress state is still rough and heterogeneous after the rupture propagation on the entire fault plane and could explain the occurrence of aftershocks just after the mainshock. This differs from the model suggested by Frankel (1991), in which a homogeneous, smooth final stress state is assumed.

A schematic model is presented in Figure 8 to describe the relationship between the initial shear strength on the fault plane and the stress drop of each subevent constituting the mainshock in a rupture cascade propagation. The antipersistent property of both the initial and final shear stress spatial correlations (i.e., scaling exponents smaller than 0.5), and more especially their identical negative Hurst exponents, is conceptualized as the sum of sine waves of amplitude to wavelength ratios more important at small scale than at larger scales. As the rupture propagates, the rupture fronts will encounter the small-scale stress variations that will form subevents and their own subevents. When each subevent

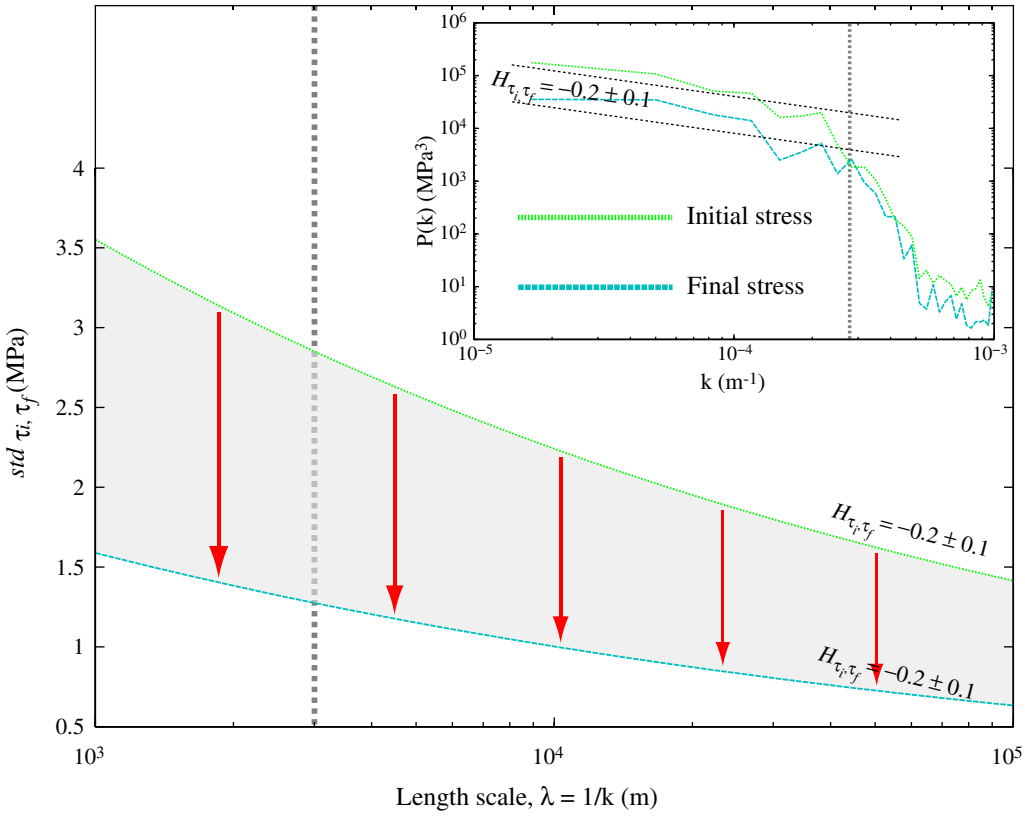

Figure 7. Standard deviation scaling of the initial and final shear strengths of the Kobe earthquake deduced from Fourier power spectra (data from Bouchon *et al.*, 1998). The second order moment of the shear strength distributions, which corresponds to the standard deviation of their spatial fluctuations, is related to the power spectra modules. Each length scale is treated as a subevent of hierarchical size constituting the whole earthquake rupture, and consequently the evolution of the stress release as a function of the subevent size is conceptualized by the vertical arrows. On both graphs the vertical dashed gray lines indicate the smallest length scale at which the stress variability is known by the seismological inversions (i.e., ~4 km). The color version of this figure is available only in the electronic edition.

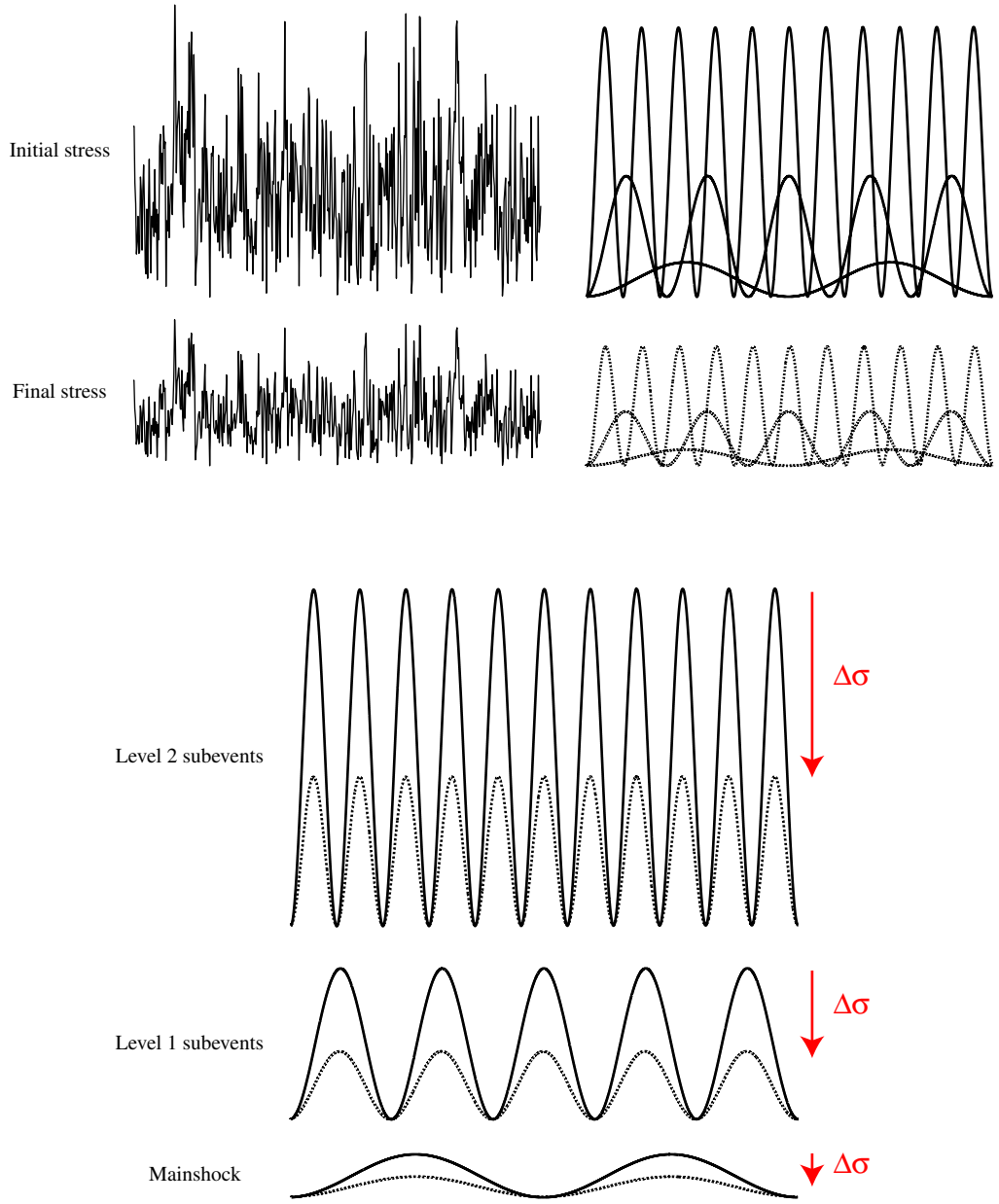

Figure 8. Schematic model explaining the relationship between the initial shear strength on the fault plane and the stress drop of each subevent constituting the mainshock in a rupture cascade propagation. The sine waves of amplitude-to-wavelength ratios are more important at small scales and depict initial and final shear stress profiles characterized by antipersistent spatial correlations. Each wavelength is assimilated to a subevent constituting the mainshock. As the rupture propagates, the smallest subevents fail, and the stress over their rupture area changes (marked by the vertical arrows) from the solid line (initial shear strength) to the dotted line (final shear strength). When the rupture continues to expand on the whole fault surface, subevents of increasing size are activated until the long and smooth wavelength shear strength constituting the mainshock is released. The color version of this figure is available only in the electronic edition.

fails, the stress over its rupture area drops from the solid line in Figure 8 to the level of dotted line. Given that this stress drop is proportional to the initial stress state, the smallest subevents bear a larger magnitude of stress change.

Finally, based on a cascade rupture model of an earthquake, and constrained by both the initial and final shear strength of the Kobe earthquake, we suggest that the stress drop averaged over the rupture area could be dependent on the size of this rupture. Given the proportionality between the initial shear strength and the stress drop, the scaling relationship reads

$$\Delta\sigma(l) \propto l^{H_R-1}, \tag{9}$$

where l corresponds to the size of the events. Note this relationship also implies that the stress-drop variability averaged over the rupture area should scale in the same way and

therefore increase as the size of the rupture area decreases. That is,

$$std_{\Delta\sigma}(l) \propto l^{H_R-1}. \tag{10}$$

Implications for Earthquake Sources Parameters: Application to the Kobe Earthquake

To illustrate the theoretical scaling relationships presented in equations (9) and (10), we consider the case of the 1995 M_L 7.2 Kobe earthquake in which the stress drop and its standard deviation averaged over the 60 km × 20 km inversion region are rather low and equal to 1.7 MPa and 0.7 MPa, respectively (Bouchon *et al.*, 1998). Approximating the rupture surface area as a disk, these two values would correspond to the average stress drop and its variability for a 20-km radius circular rupture. It would be more accurate to approximate the area of the surface rupture of the Kobe earthquake to an ellipse, but we emphasize that this assumption of a circular rupture is reasonable because we will consider small events with magnitudes smaller than 6 nucleating on the Nojima fault plane. Given this assumption, we can infer the scaling of the stress drop and its variability as a function of the radius of events nucleating on the Nojima fault plane as

$$std_{\Delta\sigma} = 37 r^{H_R-1} \tag{11}$$

and

$$\Delta\sigma = 89 r^{H_R-1}, \tag{12}$$

where r (in meters) is the radius of the rupture, and the stresses are given in MPa.

Taking $H_R = H_{||} = 0.6$ from the roughness results of the Roughness of Natural Fault Surfaces section, these scaling relationships become

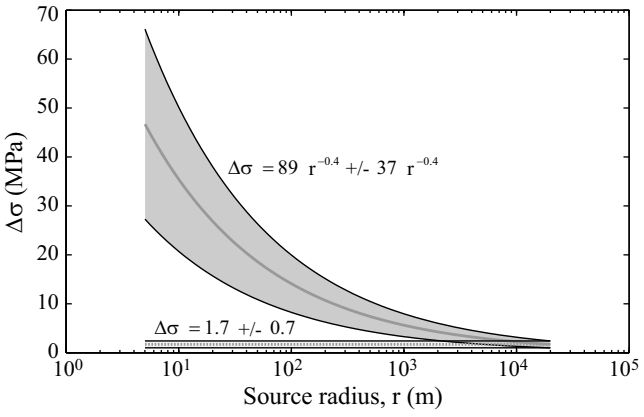

Figure 9. Theoretical scaling model of the average stress drop and its variability showing their respective evolution with the radius of ruptures nucleating on the Nojima fault plane hosting the Kobe earthquake. It is assumed that fault roughness is characterized by $H_{||} = 0.6$. The model of self-similar faulting ($H_{||} = 1$) is also shown for comparison.

$$std_{\Delta\sigma} = 37 r^{-0.4} \tag{13}$$

and

$$\Delta\sigma = 89 r^{-0.4}. \tag{14}$$

Figure 9 displays the average static stress drop and its variability as a function of the rupture radius. Whereas the average and standard deviation of the stress drop are independent of scale for a self-similar fault surface, it appears that the stress-drop fluctuations should be larger at small scales, and large stress-drop values could be reached for small earthquakes. It is important to emphasize that the scaling relationships of equations (13) and (14) have only been determined for the case of the Kobe earthquake, and the prefactors are implicitly conditioned by the values given by the seismological inversions of this event. We propose here that this behavior could be generic for earthquakes because the roughness Hurst exponents of fault surfaces and that of slip distribution are systematically measured below unity.

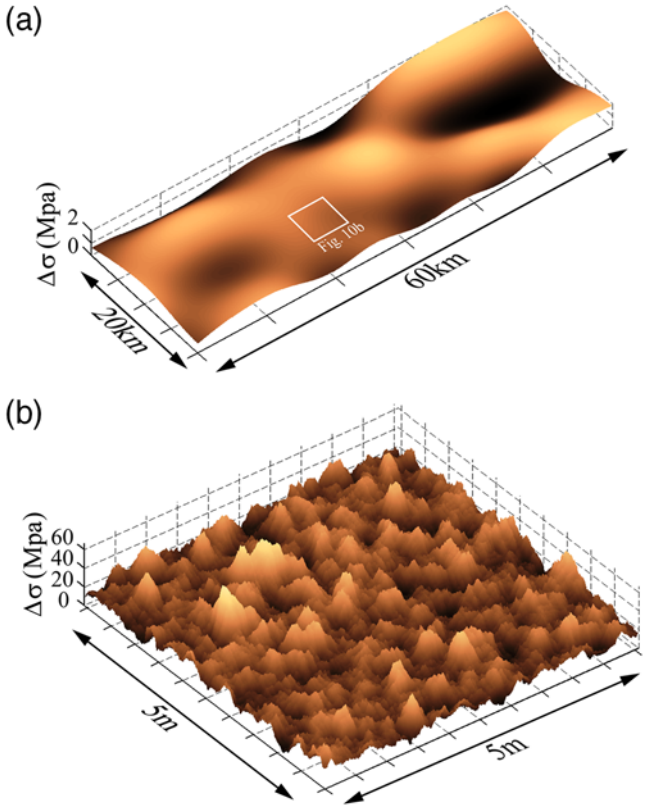

Figure 10. Map views of synthetic self-affine stress-drop distributions calculated using the theoretical scaling relationships in equations(12) and (13). (a) Smooth synthetic stress-drop field similar to the inversion results of the Kobe earthquake. The inset corresponds to the map shown on Figure 10b. (b) Magnified portion of map (a) giving access to higher stress-drop concentrations at small scales. This illustrates the stress-drop distribution inferred for a small earthquake nucleating on the Nojima fault plane. The color version of this figure is available only in the electronic edition.

Figure 10 displays map views of two realizations of synthetic fields computed with a Hurst exponent of −0.4 (corresponding to the stress drop field for $H_R = H_{||} = 0.6$). A Fourier-based method is used to simulate the isotropic self-affine matrix (Candela *et al.*, 2009). The synthetic stress drop fields are normalized to the peak amplitude of the field, which implies that areas of stress increase (negative stress drop) are not visible. Figure 10a illustrates a smooth stress-drop field at large scales with large correlated regions, similar to the inversion result of the Kobe earthquake. Because slip inversions only resolve the largest wavelengths of stress-drop fluctuations, normalized stress concentrations between 0 and 2 MPa are appropriate for this resolution. The implication is that improved resolution of slip yields higher stress-drop concentrations. This is shown on Figure 10b, which highlights a magnified area of the stress-drop field (Figure 10a) with no smoothing at small scales, and that is representative of a small earthquake nucleating on the Nojima fault plane. These realizations illustrate that large-scale fluctuations of stress drop have high-amplitude small-scale variations within them. Given our assumptions, this spatial distribution of the stress-drop field can be understood as the expression of two self-affine fault planes pressed together elastically and sheared with frictional sliding (i.e., at the Coulomb threshold).

Still considering the case of the Kobe earthquake, we estimate some commonly calculated source parameter relationships such as average static stress drop ($\Delta\sigma$), average slip (a), and area of rupture (A) versus seismic moment (M_0). The average stress drop can be written in terms of average slip and source radius (Kanamori and Anderson, 1975) as

$$\Delta\sigma = \frac{7\pi}{16} G \frac{a}{r} \tag{15}$$

and the corresponding moment (Aki, 1966) as

$$M_0 = GAa, \tag{16}$$

where G is the shear modulus. Here, $G = 30$ GPa is taken as a representative value. The average static stress drop ($\Delta\sigma$), average slip (a), and area of rupture (A) versus seismic moment (M_0) are shown in Fig. 11. We also inferred the evolution of the variability of the stress drop with the seismic moment. Combining equation (12) with equation (15), we obtain $a \propto r^{H_R}$; and, combining this last relationship with equation (15), it appears that

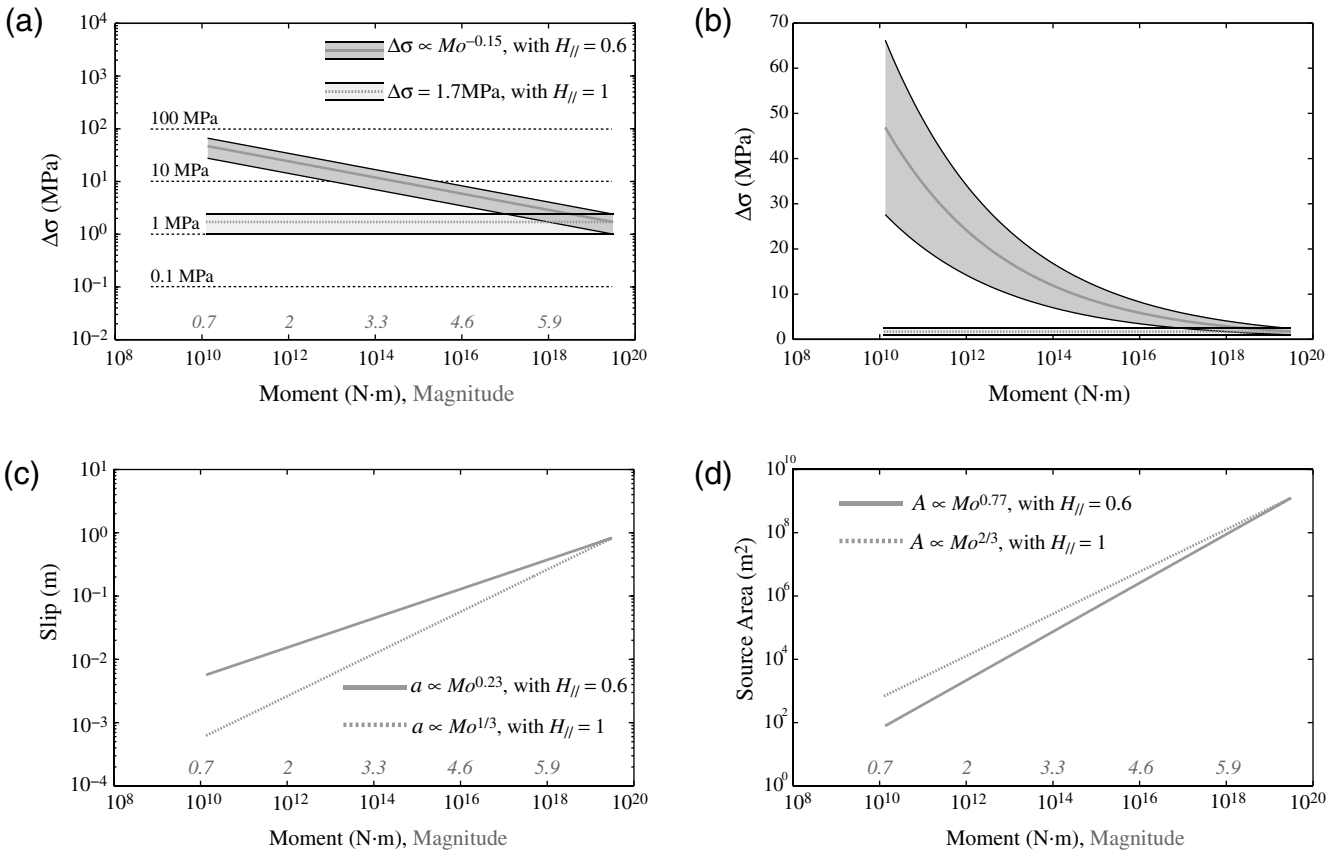

Figure 11. (a,b) Scaling relationships for the static stress drop, (c) displacement, and (d) source area with seismic moment, inferred for the Nojima fault. In (a) the horizontal dashed black lines indicate the range of seismologically observed constant average stress drop, typically between 0.1 and 100 MPa (e.g., Kanamori, 1994; Abercrombie, 1995). (b) Identical to (a) but plotted in semi-log axis to highlight the increase of the variability of the stress drop with the decrease of the seismic moment. On each graph, the scaling behavior of these source parameters is displayed as if the Nojima fault roughness was self-similar ($H_{||} = 1$) or self-affine ($H_{||} = 0.6$).

$$M_0 \propto r^{H_R+2}. \quad (17)$$

Finally, associating equation (17) with equation (12), as a consequence of the self-affine properties of the fault geometry, the faulting is not self-similar and the average strain associated with the earthquake (or equivalently the average stress) exhibits a weak dependence on the seismic moment,

$$\Delta\sigma \propto M_0^{\frac{H_R-1}{H_R+2}}. \quad (18)$$

Taking $H_R = H_{||} = 0.6$,

$$\Delta\sigma \propto M_0^{-0.15}. \quad (19)$$

Compared with self-similar faulting, our theoretical scaling model based on self-affine fault roughness with $H_{||} = 0.6$ suggests that the rupture surface area should scale strongly with slip and only weakly with seismic moment. In other words, in contrast with a self-similar faulting model where $A \propto M_0^{2/3}$ and $a \propto M_0^{1/3}$, the size of an earthquake, as measured by M_0, would be mainly controlled by the area of slip on the fault ($A \propto M_0^{0.77}$) with the amount of slip having only a weak dependence on M_0 (because $a \propto M_0^{0.23}$).

Discussion

In this investigation, we have studied the following still debated question: do earthquakes scale self-similarly, or are large earthquakes dynamically different from small ones? In our approach, the squeezing followed by the shearing of two self-affine surfaces, as would be the case for a fault interface at depth, supports the second hypothesis. The stress drop would be scale dependent and more important for small earthquakes compared to large ones. The aim in this section is to make a case for replacing previous conclusions, which usually support a self-similar faulting model, with our results and to highlight observations corroborating our findings. The limitations of our approach and the conclusions reached by our study will be exhibited with respect to the main bias inherent in the estimation of source parameters by seismological observations.

Evidences of High Stress Drop for Small Events

Our scaling model implies only a slight dependence of the stress drop on the event size (equation 12) and predicts higher values of stress drop for small events (Fig. 9) that are near the upper bound of the range of seismologically observed stress drops, typically comprised between 0.1 and 100 MPa (e.g., Kanamori, 1994; Abercrombie, 1995). Our scaling arguments (equations 11 and 12) suggest that if a small earthquake with a source radius of 5 m (i.e., a magnitude ~0.75 earthquake) would nucleate on the Nojima fault, its average stress drop would reach approximately 50± 20 MPa. This estimate is nevertheless conditioned by the low average stress drop (~1.7 MPa) over the inversion region of the Kobe earthquake (Bouchon *et al.*, 1998). Taking a rupture of similar size as the Kobe earthquake with a stress drop of 10 MPa given by the seismological inversions, our scaling model would predict a stress drop of nearly 200 ± 80 MPa, which is still close to the upper limit of the large range of seismologically observed stress drops. In addition, stress drops on the order of hundreds of MPa appear to be rare but have been observed. Munguia and Brune (1984) calculated stress drops in excess of 200 MPa for events in the 1978 Victoria, Baja California, earthquake swarm. Kanamori *et al.* (1990, 1993) estimated stress drops for a small earthquake in Pasadena, California, between 30 and 200 MPa. Imanishi and Ellsworth (2006) studied 34 M 0.2–2.1 earthquakes near Parkfield, California, from the San Andreas Fault Observatory at Depth (SAFOD) Pilot Hole array and found that half had stress drops greater than 10 MPa, with some exceeding 50 MPa.

Experimental Ruptures and Field Observations

One way to estimate if the rupture processes of small and large earthquakes are different is to attempt to bridge the gap between an experimental rupture performed in the laboratory and a natural large earthquake. The work of McGarr and Fletcher (2003) and McGarr *et al.* (2010) suggests that stick–slip friction events observed in the laboratory and earthquakes in continental settings, even with large magnitudes, have similar rupture mechanisms. McGarr and Fletcher (2003) have revealed that the maximum slips inferred for major earthquakes are consistent with those measured in the laboratory during large scale, biaxial stick-slip friction experiments (Lockner and Okubo, 1983) if differences in the state of stress and loading stiffness are taken into account. Nevertheless, it is important to note that because the friction experiments of Lockner and Okubo (1983) were conducted at low normal stress (i.e., 2.76 MPa for the rupture event analyzed by McGarr and Fletcher, 2003), the stress drop implied was also very low (~3 MPa) relative to typical measurements performed in the laboratory. Stress drops measured in triaxial experiments of shear failure of intact rocks are typically on the order of hundreds of MPa to GPa (e.g., Brace and Byerlee, 1966). Triaxial experiments with saw-cut samples have yielded slightly smaller stress drops in the range from tens to hundreds of MPa (Brace and Byerlee, 1966). In the cascade rupture model (Implication of a Rupture Cascade Model on the Variability of the Stress Drop section), faults are highly inhomogeneous and large earthquakes are composed of a number of small asperities with large stress drops within an average fault surface with a small stress drop. Therefore, the laboratory failure experiments of Brace and Byerlee (1966) are consistent with this line of thinking and suggest that stress drops during small earthquakes, constituted by single small asperities, would be relatively high.

Recently, Griffith *et al.* (2009) have proposed an alternative approach for studying the source of small earthquakes to better characterize the source dimensions and geometry

inherent to the seismological inverse problem. Using detailed field mapping of small subvertical strike-slip faults in the Lake Edison granodiorite of the central Sierra Nevada (California), they have measured the rupture length, and the slip has been identified for eight unique events. Assuming elliptical faults and using equation (15), they calculated stress drops in the range of 90 to 250 MPa for rupture radius of 8–12 m (i.e., in qualitative agreement with our theoretical estimate for earthquakes of similar size; see Fig. 9). As emphasized by Griffith *et al.* (2009), all of the coseismic slip occurred at an interface that may have represented at least a partially strong-healed asperity. This supports the argument that large earthquakes may be composed of multiscale small asperities with large stress drops. The smaller the scale of an earthquake, the more likely a single, isolated asperity is sheared.

Evolution of Stress Drop with Magnitude

Until now we have simply discussed the occurrence of high stress drop for small ruptures but not the dependence of stress drop on event size. In the case of the scaling of stress-drop variability, some recent seismological observations seem to be in agreement with the theoretical model implied by our study. Indeed, Cotton *et al.* (2008) and Akkar and Bommer (2010) observed in their set of seismological data that the ground-motion standard deviation increases when the magnitude decreases. These latter results are consistent with our results because, at first order, the ground-motion variability is dependent on stress-drop variability (Causse *et al.*, 2008).

In the case of the scaling of the average stress drop (i.e., the stress drop averaged over the rupture area), most of the studies have suggested a scale-independent behavior (e.g., McGarr, 1999; Ide and Beroza, 2001; Ide *et al.*, 2003), finding no evidence of stress drop scaling with magnitude. In particular, the work of McGarr and Fletcher (2003) points out that the maximum slip across a small area within a larger earthquake fault zone scales as the cube root of the seismic moment. This finding supports the expected relationship between slip and the seismic moment for a constant stress-drop scaling (e.g., Hanks, 1977) and departs from the relationship proposed in our model (see the Implications for Earthquake Sources Parameters: Application to the Kobe Earthquake section).

Numerous other authors (e.g., Abercrombie, 1995; Kanamori and Heaton, 2000; Brodsky and Kanamori, 2001; Prejean and Ellsworth, 2001) have presented evidence of a breakdown in constant stress parameter scaling. More precisely, using deep borehole recordings at 2.5 km depth in Cajon Pass, California, Abercrombie (1995) concluded that the apparent stress (rigidity times the ratio between seismically radiated energy to seismic moment) decreases with decreasing moment, whereas the stress drop is constant. Similar conclusions have been reached by Prejean and Ellsworth (2001) on earthquakes from M_w 0.5 to 5.0 using data from a 2-km-deep borehole in the Long Valley caldera in California. In addtion, based on the coda spectral ratio method, Mayeda *et al.* (2007) have stated that in the case of the M_w 7 Hector mine earthquake: (1) the apparent stresses are systematically lower for the moderate-size aftershocks than the mainshock, and (2) the stress drops for aftershock sizes comprised an increase of between magnitude 3.7 and 5.4. However, even if the seismological observations of Mayeda *et al.* (2007) seem robust, those of Abercrombie (1995) and Prejean and Ellsworth (2001) have been refuted by Ide *et al.* (2003). Indeed, the results of the work of Ide *et al.* (2003) indicate that frequency-dependent amplification and attenuation should be considered even for borehole observations, which was not the case in the studies of Abercrombie (1995) and Prejean and Ellsworth (2001). More especially, reexamining the data of Prejean and Ellsworth (2001), taking into account propagation effects, and making no assumption about the frequency-dependent attenuation, the most reliable measurements of Ide *et al.* (2003) follow constant stress drop and constant apparent stress scaling.

Decrease of the stress drop as a power law of the seismic moment, as suggested by equations (18) and (19), is in qualitative agreement with a study by Nadeau and Johnson (1998) of repeating earthquakes on the San Andreas fault in the Parkfield, California, area. The implied stress drops decrease from ~2000 to 100 MPa for magnitudes from ~0 to 3, whereas our model inferred from the Kobe earthquake implies a stress drop of only ~100 MPa for an event of $r \sim 0.5$ m (i.e., a magnitude of ~0). Although Sammis *et al.* (1999) argued that high stresses cannot be ruled out on physical grounds, they require perfect healing (no microscopic flaws) at the smallest asperities. We therefore suspect that the model of Nadeau and Johnson (1998) may significantly overestimate the actual stress drops associated with repeating earthquakes. In addition, the assumption of Nadeau and Johnson (1998) that the geodetically inferred slip rate on the fault plane at the surface is equal to the displacement on the smaller repeating areas of the fault at depth remains to be proven. Finally, by developing a technique to decrease uncertainties in the source parameter estimates using a borehole seismic array, Imanishi *et al.* (2004) have predicted that a repeating magnitude 2.1 earthquake was associated with a stress drop of 8.9 MPa, whereas the scaling of Nadeau and Johnson (1998) leads to a stress drop of 245 MPa for the same event.

The discussion in the previous paragraph highlights that the debate remains vigorous as to whether the seismological data tend to support a stress drop independent or dependent of the event size. The seismological observations showing that the stress drop is either constant or increases with the increase of the event size lead us to believe that other physical processes are probably activated during faulting and complicate the purely elastic scaling model proposed in our study. It is worth a note here that the previously reported increases in stress drop (e.g., Mayeda *et al.*, 2007) have been

used to argue for a fundamental change in the earthquake physics above some threshold magnitude. For instance, formation of melt associated with large slip confined to a narrow rupture zone (e.g., Di Toro and Pennacchioni, 2005), thermal pressurization (e.g., Sibson, 1973; Lachenbruch, 1980), elastohydrodynamic lubrication (Brodsky and Kanamori, 2001), or chemical decomposition (Han *et al.* 2010; De Paola *et al.*, 2011) might be expected to reduce the resistance to slip and therefore increase the stress drop. It is conceivable that these types of weakening processes alter the scaling model proposed in our study when a critical event size is reached. In other words, we suspect that the rupture physics is controlled mainly by the fault topography and, more especially, the stress drop of small earthquakes follows the scaling relationship depicted by equation (9) up to a critical size (which is difficult to precisely define).

Numerical Simulations and Dynamic Effects

Bailey and Ben-Zion (2009), using numerical simulation of evolving seismicity and stress field on a heterogeneous fault, have highlighted a similar behavior as that suggested by our study; that is the average stress drop and its variability increase when the rupture size decreases. Their simulations included fault heterogeneities modeled as heterogeneous initial shear strength and took into account dynamic overshoots (which are not considered in our present analysis). Their model showed a reduction of both variability in stress drop and its average when the earthquake size increases.

In an extended analysis of spatial correlations of slip maps for 44 earthquakes, Mai and Beroza (2002) found that the heterogeneous slip distribution follows a self-affine regime characterized by an average value $H_s = 0.71 \pm 0.23$, independent of moment magnitude or source dimensions, and is in qualitative agreement with the scaling relationship shown in equation (3). This latter observation suggests that dynamic effects produced during an earthquake might be neglected and that our scaling model highlighting the dependence of the average stress drop and its variability with the rupture size applies to seismically active faults.

Potential Biases of the Seismological Observations

There is a general lack of data where the stress drop has been computed by consistent methods over a broad magnitude range in a similar region, and scatter in the results tends to be dominated by uncertainty involved in the computation method.

As pointed out by Allmann and Shearer (2009), the computed stress drop given by slip inversions depends strongly upon modeling assumptions, especially the inherent assumption of constant rupture velocity. For example, slower rupture velocities would imply smaller estimated source radii and larger stress drops.

Prieto *et al.* (2007), in estimating source parameters from the seismic spectrum (using the idea of the jackknife variance), have revealed that it is important not only to obtain a measurement of the source parameters but also to quantify the uncertainties by means of confidence intervals. They have shown that a slight dependence of the stress drop with earthquake magnitude would pass unnoticed unless the errors are kept small. In other words, given that uncertainty in source parameter estimation is large, any slight trend of the stress drop with the rupture size would remain unnoticed.

In addition, it is important to bear in mind that, because earthquake seismology involves interpretations of elastodynamic waves, the wave field contains only indirect information about source processes (Beeler, 2006). Source physics influence the radiated field through the magnitude of several dissipative processes (for instance heat dissipation, damage, and latent heat) that reduce the radiated energy and might bias a scaling relationship between source properties and earthquake size.

To summarize, the fact that the systematic decrease in the average stress drop with magnitude is not observed as an average property in most earthquake catalogs (except for small repeating earthquake sequences) could have two origins. Either the way that the stress drops are computed may induce a large noise (as underlined by Prieto *et al.*, 2007), or some physical processes, such as off-fault damage (Dieterich and Smith, 2009), rock fragmentation and comminution, and heat dissipation during rupture, may alter both the scale dependency of the elastic stress field proposed in our study and the seismological measurements.

Conclusions

In the present study, we propose that fault-surface geometry may explain the heterogeneous patterns of seismological images of stress drop inferred from slip inversion (Bouchon, 1997; Mai and Beroza, 2002; Lavallée and Archuleta, 2005; Tinti *et al.*, 2005). We show that the spatial distribution of the stress-drop field or fault strength on a fault plane may be explained by the presence of two self-affine surfaces pressed together and sheared. This model disregards plastic processes like rock fragmentation and focuses on elastic deformation of the topography, which is the dominant mode at large scales. Given that roughness Hurst exponents of fault surfaces, as measured from field observations, are systematically below unity in different geological settings, the consequence is that the variability of the stress-drop (or its standard deviation) spatial fluctuations on the fault plane after the rupture event should increase toward small scales. Indeed kinematic rupture models are restricted to long wavelengths (typically < 1 Hzλ), and therefore the estimation of the stress-drop fluctuations along the rupture surface is limited to the largest scales, thus ignoring the largest stress variations that are expected to characterize the small scales because of the large variety of patterns of fault asperities.

Our analysis supports that the initial stress field along the fault constitutes a strong guide for the development of the earthquake and, more particularly, the stress drop. Assuming no characteristic length scale in fault roughness and a rupture

cascade model of rupture propagation, we have extrapolated the average and standard deviation stress-drop scaling behaviors toward the small earthquakes. As a direct consequence of the anti-persistent spatial correlations of the shear strength before and after the earthquake (both directly related to the elastic squeeze of fault asperities), we show that, as the rupture grows, the average stress drop and its variability should decrease with increasing source dimension or seismic moment. Therefore, faults may be considered as highly inhomogeneous with large earthquakes composed of the sum of small asperities with large stress drops within an average fault surface with small stress drop. The proposed model addresses more particularly the small to moderate-size earthquakes, that is, that we consider the rupture physics is controlled mainly by the fault topography up to a critical size where a fundamental change in the earthquake physics is expected to take place (e.g., formation of melt or another phenomena of dynamic lubrication).

Data and Resources

Stress maps of the Kobe earthquake used in this paper came from published sources listed in the references. Fault roughness data have been obtained by the authors in the field.

Acknowledgments

This study was supported by the Agence Nationale pour la Recherche grant ANR-JCJC-0011-01. Very constructive comments made by two anonymous reviewers, and Associate Editor A. McGarr helped improve the content and clarity of the manuscript. We thank Fabrice Cotton and David Marsan for fruitful discussions.

References

Abercrombie, R. E. (1995). Earthquake source scaling relationships from −1 to 5 M(L) using seismograms recorded at 2.5-km depth, *J. Geophys. Res.* **100,** 24,015–24,036.

Abercrombie, R. E., and J. R. Rice (2005). Can observations of earthquake scaling constrain slip weakening? *Geophys. J. Int.* **162,** 406–424.

Akkar, S., and J. J. Bommer (2010). Empirical equations for the prediction of PGA, PGV, and spectral accelerations in Europe, the Mediterranean region, and the Middle East, *Seismol. Res. Lett.* **81,** 2.

Aki, K. (1966). Generation and propagation of G waves from the Niigata earthquake of June 16, 1964. Part 2. Estimation of earthquake moment, release energy, and stress-strain drop from G wave spectrum, *Bull. Earthq. Res. Inst. Tokyo Univ.* **44,** 73–88.

Aki, K. (1967). Scaling law of seismic spectrum, *Bull. Seismol. Soc. Am.* **72,** 1217–1231.

Allmann, B. P., and P. M. Shearer (2007). Spatial and temporal stress-drop variations in small earthquakes near Parkfield, California, *J. Geophys. Res.* **112,** no. B04305, doi 10.1029/2006JB004395.

Allmann, B. P., and P. M. Shearer (2009). Global variations of stress drop for moderate to large earthquakes, *J. Geophys. Res.* **114,** no. B01310, doi 10.1029/2008JB005821.

Anderson, J. G. (1986). Implication of attenuation for studies of the earthquake source, in *Earthquake Source Mechanics*, S. Das, J. Boatwright, and C. H. Scholz (Editors), American Geophysical Monograph **37**, 311–318.

Anderson, J. G., and S. Hough (1984). A model for the shape of the Fourier amplitude spectrum of acceleration at high frequencies, *Bull. Seismol. Soc. Am.* **74,** 1969–1994.

Andrews, D. J. (1980). A stochastic fault model: 1. Static case, *J. Geophys. Res.* **85,** no. B7, 3867–3877, doi 10.1029/JB085iB07p03867.

Bailey, I. W., and Y. Ben-Zion (2009). Statistics of earthquake stress drops on a heterogeneous fault in an elastic half-space, *Bull. Seismol. Soc. Am.* **99,** 1786–1800, doi 10.1785/0120080254.

Barabasi, A.-L., and H. E. Stanley (1995). *Fractal Concepts in Surface Growth*, Cambridge University Press, New York, 366 pp.

Beeler, N. M. (2006). Inferring earthquake source properties from laboratory observations and the scope of lab contributions to source physics, in *Earthquakes: Radiated Energy and the Physics of Faulting*, R. E. Abercrombie, A. McGarr, H. Kanamori, and G. Di Toro, American Geophysical Monograph **170**, 81–90.

Bernard, P., A. Herrero, and C. Berge (1996). Modeling directivity of heterogeneous earthquake ruptures, *Bull. Seismol. Soc. Am.* **86,** 1149–1160.

Bistacchi, A., W. A. Griffith, S. A. F. Smith, G. Di Toro, R. Jones, and S. Nielsen (2011). Fault roughness at seismogenic depths from LIDAR and photogrammetric analysis, *Pure Appl. Geophys.* doi 10.1007/s00024-011-0301-7.

Boatwright, J., J. B. Fletcher, and T. E. Fumal (1991). A general inversion scheme for source, site, and propagation characteristics using multiply recorded sets of moderate-sized earthquakes, *Bull. Seisml. Soc. Am.* **81,** 1754–1782.

Bouchon, M. (1997). The state of stress on some faults of the San Andreas system as inferred from near-field strong motion data, *J. Geophys. Res.* **102,** 11,731–11,744, doi 10.1029/97JB00623.

Bouchon, M., H. Sekiguchi, K. Irikura, and T. Iwata (1998). Some characteristics of the stress field of the 1995 Hyogo-ken Nanbu (Kobe) earthquake, *J. Geophys. Res.* **103,**, no. B10, 24,271–24,282, doi 10.1029/98JB02136.

Brace, W. F., and J. Byerlee (1966). Stick-slip as a mechanism for earthquakes, *Science* **153,** 990–992, doi 10.1126/science.153.3739.990.

Brodsky, E. E., and H. Kanamori (2001). Elastohydrodynamic lubrication of faults, *J. Geophys. Res.* **106,** no. B8, 16,357–16,374.

Brodsky, E. E., and J. Mori (2007). Creep events slip less than ordinary earthquakes, *Geophys. Res. Lett.* **34,** L16309, doi 10.1029/2007GL030917.

Brodsky, E. E., J.G. Gilchrist, A. Sagy, and C. Colletini (2011). Faults smooth gradually as a function of slip, *Earth Planet. Sci. Lett.* **302,** 185–193, doi 10.1016/j.epsl.2010.12.010.

Candela, T., F. Renard, M. Bouchon, D. Marsan, J. Schmittbuhl, and C. Voisin (2009). Characterization of fault roughness at various scales: Implications of three-dimensional high resolution topography measurements, *Pure Appl. Geophys.* **166,** 1817–1851.

Causse, M., F. Cotton, C. Cornou, and P.-Y. Bard (2008). Calibrating median and uncertainty estimates for a practical use of empirical Green's functions technique, *Bull. Seismol. Soc. Am.* **98,** 344–353, doi 10.1785/0120070075.

Causse, M., F. Cotton, and P. M. Mai (2010). Constraining the roughness degree of slip heterogeneity, *J. Geophys. Res.* **115,** no. B05304, doi 10.1029/2009JB006747.

Choy, G. L., and S. H. Kirby (2004). Apparent stress, fault maturity and seismic hazard for normal-fault earthquakes at subduction zones, *Geophys. J. Int.* **159,** no. 3, 991–1012, doi 10.1111/j.1365-246X.2004.02449.x.

Cotton, F., G. Pousse, F. Bonilla, and F. Scherbaum (2008). On the discrepancy of recent European ground-motion observations and predictions from empirical models: Analysis of KiK-net accelerometric data and point-sources stochastic simulations, *Bull. Seismol. Soc. Am.* **98,** no. 5, 2244–2261.

Dieterich, J. H., and D. E. Smith (2009). Nonplanar faults: Mechanics of slip and off-fault damage, *Pure Appl. Geophys.* **166,** 1799–1815.

De Paola, N., T. Hirose, T. Mitchell, G. Di Toro, C. Viti, and T. Shimamoto (2011). Fault lubrication and earthquake propagation in thermally unstable rocks, *Geology* **39,** 35–38, doi 10.1130/G31398.1.

Di Toro, G., and G. Pennacchioni (2005). Fault plane processes and mesoscopic structure of a strong-type seismogenic fault in tonalites (Adamello batholith, Southern Alps), *Tectonophysics* **402,** 55–80.

Fonseca, J. (1988). The Sou Hills: A barrier to faulting in the central Nevada seismic belt, *J. Geophys. Res.* **93,** no. B1, 475–489.

Frankel, A. (1991). High-frequency spectral fall-off of earthquakes, fractal dimension of complex rupture, *b* value, and the scaling of strength on faults, *J. Geophys. Res.* **96,** no. B4, 6291–6302, doi 10.1029/91JB00237.

Frankel, A., and L. Wennerberg (1989). Microearthquake spectra from the Anza, California, seismic network: Site response and source scaling, *Bull. Seismol. Soc. Am.* **79,** no. 3, 581–609.

Griffith, W. A., G. Di Toro, G. Pennacchioni, D. D. Pollard, and S. Nielsen (2009). Static stress drop associated with brittle slip events on exhumed faults, *J. Geophys. Res.* **114,** no. B02402, doi 10.1029/2008JB005879.

Han, R., T. Hirose, and T. Shimamoto (2010). Strong velocity weakening and powder lubrication of simulated carbonate faults at seismic slip rates, *J. Geophys. Res.* **115,** no. B03412, doi 10.1029/2008JB006136.

Hanks, T. C. (1977). Earthquake stress drops, ambient tectonic stresses and stresses that drive plate motions, *Pure Appl. Geophys.* **115,** 441–458.

Hanks, T. C. (1982). $f_{\max}$, *Bull. Seismol. Soc. Am.* **72,** 1867–1879.

Ide, S., and G. C. Beroza (2001). Does apparent stress vary with earthquake size? *Geophys. Res. Lett.* **28,** 3349–3352.

Ide, S., G. C. Beroza, S. G. Prejean, and W. L. Ellsworth (2003). Apparent break in earthquake scaling due to path and site effects on deep borehole recordings, *J. Geophys. Res.* **108,** no. 2271, doi 10.1029/2001JB001617.

Imanishi, K., and W. L. Ellsworth (2006). Source scaling relationships of microearthquakes at Parkfield, CA, determined using the SAFOD Pilot Hole seismic array, in *Earthquakes: Radiated Energy and the Physics of Faulting*, R. E. Abercrombie, A. McGarr, H. Kanamori, and G. Di Toro (Editors), American Geophysical Monograph **170**, 81–90.

Imanishi, K., W. L. Ellsworth, and S. G. Prejean (2004). Earthquake source parameters determined by the SAFOD Pilot Hole seismic array *Geophys. Res. Lett.* **31,** L12S09, doi 10.1029/2004GL019420.

Kanamori, H. (1994). Mechanics of earthquakes, *Ann. Rev. Earth Planet. Sci.* **22,** 207–237, doi 10.1146/annurev.ea.22.050194.001231.

Kanamori, H., and D. L. Anderson (1975). Theoretical basis of some empirical relations in seismology, *Bull. Seismol. Soc. Am.* **65,** 1073–1095.

Kanamori, H., and E. E. Brodsky (2004). The physics of earthquakes, *Rep. Prog. Phys.* **67,** 1429–1496.

Kanamori, H., and T. H. Heaton (2000). Microscopic and macroscopic physics of earthquakes, in *GeoComplexity and the Physics of Earthquakes*, J. Rundle, D. Turcotte, and W. Klein (Editors), American Geophysical Monograph **120,** 147–183.

Kanamori, H., J. Mori, and T. H. Heaton (1990). The 3 December 1988, Pasadena earthquake ($M_L = 4.9$) recorded with the very broadband system in Pasadena, *Bull. Seismol. Soc. Am.* **80,** 483–487.

Kanamori, H., J. Mori, E. Hauksson, T. H. Heaton, L. K. Hutton, and L. M. Jones (1993). Determination of earthquake energy release and M_L using TERRAscope, *Bull. Seismol. Soc. Am.* **2,** 330–346.

Lachenbruch, A. H. (1980). Frictional heating, fluid pressure, and the resistance to fault motion, *J. Geophys. Res.* **85,** no. B11, 6097–6112, doi10.1029/JB085iB11p06097.

Lavallée, D., and R. J. Archuleta (2005). Coupling of the random properties of the source and the ground motion for the 1999 Chi Chi earthquake *Geophys. Res. Lett.* **32,** L08311, doi 10.1029/2004GL022202.

Lee, J. J., and R. L. Bruhn (1996). Structural anisotropy of normal fault surfaces, *J. Struct. Geol.* **18,** 1043–1059.

Lockner, D. A., and P. G. Okubo (1983). Measurements of frictional heating in granite, *J. Geophys. Res.* **88,** no. B5, 4313–4320, doi 10.1029/JB088iB05p04313.

Mai, P. M., and G. C. Beroza (2002). A spatial random field model to characterize complexity in earthquake slip, *J. Geophys. Res.* **107,** no. 2308, doi 10.1029/2001JB000588.

Marsan, D. (2006). Can coseismic stress variability suppress seismicity shadows? Insights from a rate-and-state friction model, *J. Geophys. Res.* **111,** no. B06305, doi 10.1029/2005JB004060.

Mayeda, K., L. Malagnini, and W. R. Walter (2007). A new spectral ratio method using narrow band coda envelopes: Evidence for non-self-similarity in the Hector Mine sequence, *Geophys. Res. Lett.* **34,** L11303, doi 10.1029/2007GL030041.

McGarr, A. (1999). On relating apparent stress to the stress causing earthquake fault slip, *J. Geophys. Res.* **104,** no. B2, 3003–3011, doi10.1029/2007GL030041.

McGarr, A., and J. B. Fletcher (2003). Maximum slip in earthquake fault zones, apparent stress, and stick-slip friction, *Bull. Seismol. Soc. Am.* **93,** 2355–2362.

McGarr, A., J. B. Fletcher, M. Boettcher, N. Beeler, and J. Boatwright (2010). Laboratory-based maximum slip rates in earthquake rupture zones and radiated energy, *Bull. Seismol. Soc. Am.* **100,** 3250–3260, doi 10.1785/0120100043.

Meakin, P. (1998). *Fractals: Scaling and Growth Far from Equilibrium*, Cambridge University Press, New York, 674 pp.

Méheust, Y., and J. Schmittbuhl (2003). Scale effects related to flow in rough fractures, *Pure Appl. Geophys.* **160,** 1023–1050.

Munguia, L., and J. N. Brune (1984). High stress-drop events in the Victoria, Baja California earthquake swarm of 1978 March, *Geophys. J. Roy. Astron. Soc.* **76,** no. 3, 725–752, doi 10.1111/j.1365-246X.1984.tb01919.x.

Nadeau, R. M., and L. R. Johnson (1998). Seismological studies at Parkfield VI: Moment release rates and estimates of source parameters for small repeating earthquakes, *Bull. Seismol. Soc. Am.* **88,** 790–814.

Okaya, D. A., and G. A. Thompson (1985). Geometry of Cenozoic extensional faulting: Dixie Valley, Nevada, *Tectonics* **4,** 107–125.

Power, W. L., and W. B. Durham (1997). Topography of natural and artificial fractures in granitic rocks: Implications for studies of rock friction and fluid migration, *Int. J. Rock Mech. Min. Sci.* **34,** 979–989.

Power, W. L., and T. E. Tullis (1989). The relationship between slickenside surfaces in fine-grained quartz and the seismic cycle, *J. Struct. Geol.* **11,** 879–893.

Power, W. L., and T. E. Tullis (1991). Euclidean and fractal models for the description of rock surface roughness, *J. Geophys. Res.* **96,** no. 1, 415–424, doi 10.1029/90JB02107.

Power, W. L., and T. E. Tullis (1992). The contact between opposing fault surfaces at Dixie Valley, Nevada, and implications for fault mechanics, *J. Geophys. Res.* **97,** no. B11, 15,425–15,435, doi 10.1029/92JB01059.

Power, W. L., T. E. Tullis, S. R. Brown, G. N. Boitnott, and C. H. Scholz (1987). Roughness of natural fault surfaces, *Geophys. Res. Lett.* **14,** 29–32.

Power, W. L., T. E. Tullis, and J. D. Weeks (1988). Roughness and wear during brittle faulting, *J. Geophys. Res.* **93,** no. B12, 15,268–15,278, doi 10.1029/JB093iB12p15268.

Prejean, S. G., and W. L. Ellsworth (2001). Observations of earthquake source parameters and attenuation at 2 km depth in the Long Valley caldera, eastern California, *Bull. Seismol. Soc. Am.* **91,** 165–177.

Prieto, G. A., P. M. Shearer, F. L. Vernon, and D. Kilb (2004). Earthquake source scaling and self-similarity estimation from stacking *P* and *S* spectra, *J. Geophys. Res.* **109,** no. B08310, doi 10.1029/2004JB003084.

Prieto, G. A., D. J. Thomson, F. L. Vernon, P. M. Shearer, and R. L. Parker (2007). Confidence intervals for earthquake source parameters, *Geophys. J. Int.* **168,** 1227–1234.

Renard, F., C. Voisin, D. Marsan, and J. Schmittbuhl (2006). High resolution 3D laser scanner measurements of a strike-slip fault quantify its morphological anisotropy at all scales, *Geophys. Res. Lett.* **33,** L04305, doi 10.1029/2005GL025038.

Sagy, A., E. E. Brodsky, and G. J. Axen (2007). Evolution of fault-surface roughness with slip, *Geology* **35,** 283–286.

Sammis, C. G., R. M. Nadeau, and L. R. Johnson (1999). How strong is an asperity? *J. Geophys. Res.* **104,** no. B5, 10,609–10,619, doi 10.1029/1999JB900006.

Schmittbuhl, J., and J. Vilotte (1999). Interfacial crack front wandering: Influence of correlated quenched noise, *Physica A* **270,** 42–56.

Schmittbuhl, J., G. Chambon, A. Hansen, and M. Bouchon (2006). Are stress distributions along faults the signature of asperity squeeze? *Geophys. Res. Lett.* **33,** L13307, doi 10.1029/2006GL025952.

Schmittbuhl, J., A. Delaplace, K. Maloy, H. Perfettini, and J. Vilotte (2003). Slow crack propagation and slip correlations, *Pure. Appl. Geophys.* **160,** 961–976, doi 10.1007/PL00012575.

Schmittbuhl, J., S. Gentier, and R. Roux (1993). Field measurements of the roughness of fault surfaces, *Geophys. Res. Lett.* **20,** no. 8, 639–641, 10.1029/93GL00170.

Scholz, C. H. (2002). *The Mechanics of Earthquakes and Faulting*, Second Ed., Cambridge University Press, New York, 496 pp.

Shearer, P. M., G. A. Prieto, and E. Hauksson (2006). Comprehensive analysis of earthquake source spectra in southern California, *J. Geophys. Res.* **111,** no. B06303, doi 10.1029/2005JB003979.

Sibson, R. H. (1973). Interactions between temperature and fluid during earthquake faulting: A mechanism for partial or total stress relief, *Nature* **243,** 66–68.

Singh, S., and G. Suárez (1988). Regional variation in the number of aftershocks ($m_b \geqq 5$ of large, subduction-zone earthquakes ($M_w \geqq 7.0$), *Bull. Seismol. Soc. Am.* **78,** no. 1, 230–242.

Thouvenot, F. (1998). The M_L 5.3 Epagny (French Alps) earthquake of 1996 July 15: A long-awaited event on the Vuache fault, *Geophys, J. Int.* **135,** 876–892.

Tinti, E., P. Spudich, and M. Cocco (2005). Earthquake fracture energy inferred from kinematic rupture models on extended faults, *J. Geophys. Res.* **110,** no. B12303, doi 10.1029/2005JB003644.

Venkataraman, A., and H. Kanamori (2004). Observational constraints on the fracture energy of subduction zone earthquake, *J. Geophys. Res.* **109,** no. B05302, doi 10.1029/2003JB002549.

ISTerre, CNRS & University Joseph Fourier
Grenoble I, OSUG, BP 53
38041 Grenoble, France
thibault.candela@ujf-grenoble.fr
francois.renard@ujf-grenoble.fr
michel.bouchon@ujf-grenoble.fr
(T.C., F.R., M.B.)

Institut de Physique du Globe de Strasbourg (UMR 7516)
5, rue René Descartes
67084 Strasbourg Cedex
Strasbourg, France
Jean.Schmittbuhl@eost.u-strasbg.fr
(J.S.)

Department of Earth and Planetary Sciences
University of California—Santa Cruz
Santa Cruz, California 95064
ebrodsky@es.usc.edu
(E.E.B.)

Manuscript received 27 October 2010